DIPLOMARBEIT

am Leibniz-Institut für Atmosphärenphysik in Kühlungsborn
an der Universität Rostock

Analysis of Simultaneous Wind Measurements in the Mesosphere Using Doppler-Wind Lidar and Rocketsondes

von
Marin Stanev

Abstract: This study compares wind soundings performed with rocketsondes and Doppler-wind lidar in the middle atmosphere. The summer rocket campaign as part of the WADIS research project at the Andøya Rocket Range in Norway (69°N 16°E) consisted of 1 launch of an instrumented sounding rocket and 11 launches of smaller meteorological rockets carrying datasonde payloads.

Datasondes measure temperature and wind in the altitude range between 20 km and 70 km. The trajectory is tracked by radar. The ALOMAR RMR-Lidar consists of two pulsed laser beams and two telescopes that can be tilted in North-West (NWT) and South-East (SET) direction.

The launches in the time period of June 26. - July 1. 2013 were accompanied by concurrent ground-based lidar- and radar-measurements. Lidar and datasonde wind measurements were in a quasi common volume in the case of the NWT telescope at a distance of less than 1 km at 54 km altitude, while the SET telescope pointed away from the datasonde trajectory at a distance of approx. 20 km at 50 km altitude. Higher radar tracking resolution of 50 Hz allowed an improved estimation of the datasonde wind errors. The new datasonde analysis software is consistent with previous analysis methods with a difference of less than 0.6 m/s under certain conditions.

On the night of the 30.06. / 01.07.2013, close agreement between the lidar and datasonde wind measurements has been shown in the altitude range between 45 km and 65 km. The comparison of lidar, datasonde and MF radar wind measurements during the rocket launch on the 01.07.2013 at 0:30 UT show excellent agreement in the altitude range of 45 km - 70 km. Better agreement in the line-of-sight wind measurements of the NWT lidar telescope has been shown than in the zonal wind measurements of the SET lidar telescope.

Postal address:
Schloss-Str. 6
18225 Kühlungsborn
Germany

IAP Kühlungsborn
Mai 2014
IAP Nr. 39/2014
ISSN 1615-8083

LEIBNIZ-INSTITUT FÜR ATMOSPHÄREN PHYSIK IAP

Analysis of Simultaneous Wind Measurements in the Mesosphere Using Doppler-Wind Lidar and Rocketsondes

von
Marin Stanev

Dieser Forschungsbericht wurde als Diplomarbeit vom Fachbereich Physik an der Mathematisch-Naturwissenschaftlichen Fakultät der Universität Rostock angenommen.

Gutachter: Prof. Dr. Franz-Josef Lübken
Dr. Gerd Baumgarten

verteidigt am: 16. Mai 2014

Contents

1 Introduction

1.1 Motivation

The ALOMAR RMR lidar located near Andenes in Norway went into operation in June 1994. Since then, it has measured temperature profiles and aerosol properties in the strato- and mesosphere (*Schöch*, 2007). In 2009, the addition of the Doppler-Rayleigh-Iodine Spectrometer ("DoRIS") allowed the simultaneous measurement of temperature and wind speeds in the middle atmosphere (*Baumgarten*, 2010). This study builds on the work done by Jens Hildebrand and Gerd Baumgarten to systematically compare independent wind retrieval methods in order to estimate the accuracy of the new instrument (*Hildebrand et al.*, 2012; *Hildebrand*, 2014). While the advantages of lidar wind measurements such as long observation times in fair weather and comparatively low cost and necessary supervision in respect to rocket soundings mean that it can be used in situations in which other methods are not available, an estimate of the systematic bias, if it exists, would prove useful in the analysis of its results.

The goal of this thesis is to compare the accuracy of remote sensing and in-situ measurements of wind speed in the middle atmosphere. The measurements are performed using the ALOMAR RMR-Lidar and Radar-tracking of a falling datasonde at the Andøya Rocket Range. During the WADIS rocket campaign, 11 meteorological rockets were launched in a period of 5 days. Simultaneous measurements of wind speed with the DoRIS instrument and the derivation of background winds from the datasonde trajectories during the campaign allow a qualitative judgment of each methods advantages and disadvantages. An estimate of the error ranges of the DoRIS instrument is of particular interest.

1.2 Structure of this thesis

In chapter 2 there is a brief overview of the thermal structure of the atmosphere, including phenomena such as atmospheric waves affecting the dynamics of the vertical layers of air. An overview of wind speed measuring methods is given in chapter 3. The experimental specifics of the equipment and the physical approximations used in this study are enumerated in chapter 4. The actual conditions and proceedings of the WADIS campaign are listed in chapter 5, including the results of the rocket measurements. Chapter 6 features a discussion of the lidar data collected during the WADIS campaign. That data is compared to the datasonde soundings and to past studies. Possible systematic and random error sources are discussed for each method in chapters 5 and 6, respectively. In conclusion, chapter 7 gives a summary of this study and an outlook towards future areas of investigation.

2 Theory

2.1 Fundamentals of atmospheric physics

The early earth's atmosphere was a unique gaseous layer resulting from the interplay between a reducing mixture of water vapor (H_2O), carbon monoxide (CO), carbon dioxide (CO_2), hydrochloric acid (HCl), methane (CH_4), ammonia (NH_3), nitrogen (N_2), sulfur gases and simple organisms engaged in photosynthesis (*Kasting*, 1993). A process started approximately 4 billion years ago led to a self-sustaining habitable environment, whose structure and dynamics are of great relevance to humanity. In the following chapter, an overview of the current, commonly accepted classification of the atmospheric layers and their interaction will be given.

2.2 Thermic structure of the polar atmosphere

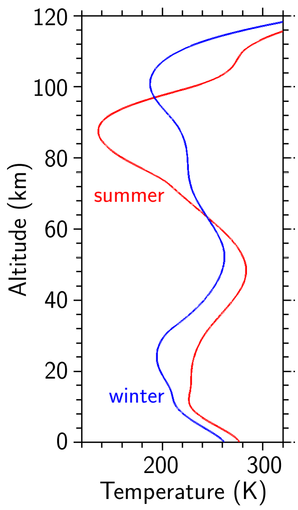

Figure 2.1: Vertical profile of atmospheric temperature for summer and winter. The temperature profiles are extracted from the NRLMSISE-00 reference atmosphere (*Picone et al.*, 2002). The summer profile (red) corresponds to July 1st, the winter profile (blue) to January 1st at the location of ALOMAR (69° N, 16° E). Figure is adapted from *Hildebrand* (2014).

The composition of the atmosphere is regarded as roughly constant up to a height above sea level of 100 km. This volume is called the homosphere. It consists of 78% N_2, 21% O_2, 1% Ar and aerosols including H_2O and O_3. Above the homospere lies the heterosphere, in which diffusive demixing alters the composition significantly. The vertical segmentation of the atmosphere is usually given respective to the vertical temperature gradient (see figure 2.1). Periods of temperature gradient reversal are referred to as *pauses*. The region of 0-8 km has a negative temperature gradient of -6 K/km up to -10 K/km due to heating from the earth's surface and is referred to as the troposphere. Mixing of this layer can occur, if the temperature gradient has a steeper decline than the adiabatic temperature gradient. Almost the entire H_2O content in the atmosphere is contained inside the troposphere, leading to condensation as a consequence of mechanical convection. This process is called precipitation.

Following the tropopause above 10 km, the dominant energy transportation mechanism changes from convection to heat radiation inside the atmosphere. We observe a positive temperature gradient in a region called the stratosphere (10-50 km) due to the volume concentration of O_3, which rises up to approximately 8 ppmv in 35 km height. Solar UV-B radiation leads to dissociation and recombination of the molecule as part of the Chapman-Cycle (*Finlayson-Pitts and James N Pitts*, 1999). The molecular collisions that are a part of this cycle cause heating. A positive temperature gradient leads to a stable layering inside the stratosphere, thereby minimizing mixing.

Temperature falls above the stratopause due to the lack of heating mechanisms until it reaches a global minimum between 85 and 100 km varying with latitude and season. During polar summer, the temperatures reach down to 130 K.

Above the mesopause, temperature rises more than 1000 K in the so called thermospere due to photodissociation of molecular N_2 and O_2. The atmospheric density falls off exponentially, leading to ineffective heat transport and a sharp positive temperature gradient.

2.3 Wind structure of the polar atmosphere

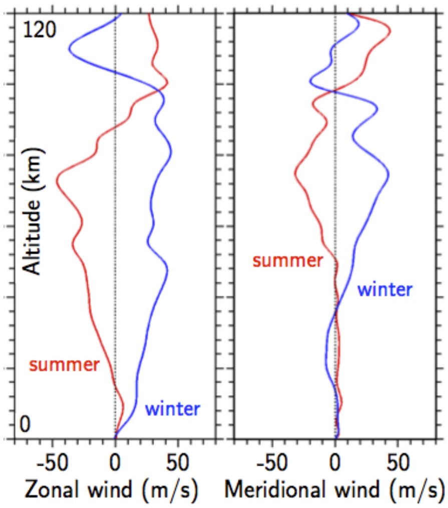

Figure 2.2: Vertical profiles of zonal and meridional wind for summer and winter. The wind speed profiles are extracted from the HWM07 model (*Drob et al.*, 2008). The summer profiles (red) correspond to July 1st, the winter profiles (blue) to January 1st at the location of ALOMAR (69° N, 16° E). Figure is adapted from (*Hildebrand*, 2014)

In polar latitudes, certain recurring annual features can be identified (see figure 2.2). The so-called polar vortex is an eastward wind current during winter conditions with its highest speed around the stratopause (*Brekke*, 2012). The wind direction reverses around the mesopause. In summer conditions the wind direction is westward in the strato- and mesosphere, with a maximum in the mesosphere. Meridional wind streams southward during summer and northward during winter, again with a maximum in the mesosphere.

2.4 Dynamics equations

In order to discuss the wave dynamics in the atmosphere, it is necessary to introduce the concepts of potential temperature Θ and vorticity $rot(\vec{s})$. The potential temperature Θ is used as a substitute for altitude designations and is defined as the temperature a dry packet of air would possess, if it were lowered adiabatically from a given height to a reference pressure p_0, i.e. sea level. It is calculated according to:

$$\Theta(z) = T(z)(\frac{p_0}{p(z)})^{1-\frac{1}{\gamma}} \tag{2.1}$$

The adiabatic coefficient $\gamma = \frac{c_p}{c_v}$ is calculated from the specific heat and its value is ≈ 1.4 for air. The potential temperature Θ is a conserved quantity in adiabatic processes and used to refer to isentropic vertical layers.

We use spherical coordinates for wind speed u,v and w, pointing respectively in the zonal, meridional and vertical direction. Observing physical processes inside a comoving spherical coordinate system leads to the appearance of pseudo forces when converting the original description from an inertial frame of reference. Wind streams inside a spherical hull around earth are a relevant example, and to calculate their contribution we assume that $w = 0$ and the horizontal components of this idealized flow do not depend on z ($\frac{\partial u}{\partial z} = \frac{\partial v}{\partial z} = 0$). Calculating the components of the vorticity $rot(\vec{s})$ in euclidean coordinates yields:

$$rot(\vec{s}) = \vec{\nabla} \times \vec{s} = \xi \vec{e_x} + \eta \vec{e_y} + \zeta \vec{e_z} \tag{2.2}$$

$$\xi = \frac{\partial w}{\partial y} - \frac{\partial v}{\partial z}$$

$$\eta = \frac{\partial u}{\partial z} - \frac{\partial w}{\partial x}$$

$$\zeta = \frac{\partial \mathrm{v}}{\partial x} \text{-} \frac{\partial u}{\partial y}$$

It follows that $rot(\vec{s}) = \zeta \vec{e_z}$, hence the rotation is perpendicular to the x-y-plane.

Applying these relations to a rotating coordinate system, we evaluate the composite motion $\vec{s_a} = \vec{s} + \vec{s_e}$, where $\vec{s}$ is the motion relative to the earth and $\vec{s_e} = \vec{\omega} \times \vec{r}$ the motion of the earth itself ($\vec{r}$ is the radius and $\vec{\omega}$ the angular velocity of the earth). Inserting $\vec{s_a}$ in (2.2) and using the relation $\vec{\nabla} \times (\vec{\omega} \times \vec{r}) = 2\vec{\omega}$ leads to

$$\zeta_a = \zeta + 2\omega \sin\phi = \zeta + f \tag{2.3}$$

f is called the Coriolis-parameter and ϕ is the geographic latitude. The vorticity $rot(\vec{s})$ is conserved under a horizontal, divergence-free flow when neglecting friction (*Visconti*, 2001).

2.5 Atmospheric waves

Periodic wave-like motions of air can be observed in the atmosphere from wavelengths of the order of centimeters (sonic waves), to 10-100 km (gravity waves) and more than 1000 km (planetary waves). In order to describe the motion, it is sufficient to consider a packet of air and sum over all the forces influencing its movement. The resulting equation contains the dynamics according to Newton's second law.

$$\frac{d}{dt} mv = \sum_i \vec{F_i} \tag{2.4}$$

There are four relevant forces: gravity F_G, Coriolis force F_C, pressure gradient F_p and friction F_R.

$$F_G = -m\vec{g}$$

If the packet of air is disturbed vertically and out of equilibrium with its environment, the buoyancy force $F_A = \Delta m\vec{g}$ will cause oscillations of the order of minutes till days.

These oscillations are referred to as gravity waves. The wave equation when neglecting F_C and F_R is

$$\frac{d^2z}{dt^2} = -g(\frac{\Gamma - \gamma}{T_0})$$

In this case, Γ is the adiabatic temperature gradient, γ is the background temperature gradient and T_0 the temperature of the packet originally in equilibrium. The frequency of this oscillation $N^2 = g(\frac{\Gamma-\gamma}{T_0})$ is called the Brunt-Väisälä-frequency and for positive values a measure of the stability of atmospheric layers. It is possible to express it with the potential temperature defined in equation (2.1) (*Ambaum*, 2010):

$$N = \sqrt{\frac{g}{\Theta}\frac{\partial\Theta}{\partial z}} \tag{2.5}$$

$$F_C = -2m\vec{\omega} \times \vec{v}$$

The Coriolis force follows from our observation of movement inside a rotating sphere (see Dynamics equations) and is perpendicular to the radial direction. Moving the air packet in the meridional direction across long scale distances (order of 1000 km) leads to the development of planetary or Rossby-waves.

Sound waves develop horizontally analogous to gravity waves in the direction of high to low atmospheric pressure. The wavelength of these waves is of the order of centimeters and rarely considered due to their fast dissipation. Pressure in the measurements is assumed to be constant across the lateral direction, hence we neglect the force F_p in the further discussion.

Friction occurs in boundary layers, due to shearing stress and particularly at high altitudes. It is not a corrective force, but proportional to velocity $\vec{v}$. Instead of an analytical term, we approximate the various effects in a cartesian coordinate system with $F_{R_x}, F_{R_y}, F_{R_z}$.

Solving this equation in earth-bound coordinates u, v, w with the atmospheric density ρ and geographical latitude ϕ leads us to the Navier-Stokes-equation in 3 dimensions (*Salby*, 1996).

$$\begin{aligned}\frac{du}{dt} &= -\frac{1}{\rho} + 2\omega(v\sin\phi - w\cos\phi) + F_{R_x}\\ \frac{dv}{dt} &= -\frac{1}{\rho} - 2\omega\sin\phi + F_{R_y}\\ \frac{dw}{dt} &= -\frac{1}{\rho} - g + 2\omega u\cos\phi + F_{R_z}\end{aligned} \tag{2.6}$$

This is a non-linear differential equation and has no general analytical solution. Evaluating the contributing parameters and linearising lets us derive particular solutions.

Conservation of energy inside the wave dynamics leads to an increasing amplitude with altitude, as the atmospheric density decreases exponentially.

$$A(z) = A_0 e^{(\frac{z-z_0}{2H})} \qquad H = \frac{k_B T}{mg}$$

H is the scale height, which approximates the loss of air pressure by a constant e in the vertical direction at a constant temperature. In the terrestrial atmosphere its value is $H \approx 7$ km.

2.6 Gravity waves

Relevant to our study are two cases of gravity waves: tidal waves, which have a diurnal cycle due to heating by solar radiation, and smaller-scale gravity waves due to orographic excitation on the lee side of mountains (*Chapman and Lindzen*, 1970).

The dispersion relation for internal waves when only including the gravitational force F_G in the Navier-Stokes-Equations (2.6) is (*Fritts*, 2003):

$$m^2 = \frac{(k^2 + l^2)(N^2 - \hat{\omega^2})}{(\hat{\omega}^2 - f^2)} - \frac{1}{4H^2}$$

$$\hat{\omega} = \omega - k\bar{u} - l\bar{v}$$

The following variables are used: H ist the scale height, f is the Coriolis parameter, N is the Brunt-Väisälä frequency, $\hat{\omega}$ is the intrinsic frequency, which is independent from the background zonal and meridional wind $\bar{u}, \bar{v}$ and k, l, m are the zonal, meridional and vertical wavenumbers respectively. In our case, the intrinsic frequency lies in the range of $N \gg \hat{\omega} \gg f$, which simplifies the dispersion relation to (*Fritts*, 2003):

$$|m| = \frac{N}{|c_h - \bar{u_h}|} \tag{2.7}$$

In this case, c_h is the horizontal phase velocity and $\bar{u_h}$ the mean horizontal wind speed. If $c_h = \bar{u_h}$, the critical level, the vertical wavelength reaches $\lambda_z = 0$. This represents an upper bound on the wind speed. In practice, the maximum observed wind speed is lower.

2.7 Spectral power density

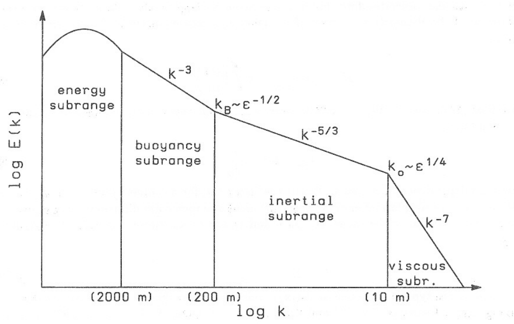

Figure 2.3: Power spectral density regimes depending on vertical wave number k (*Lübken*, 1993).

Gravity waves are excited and travel from the troposphere to the mesosphere, where they break and dump their momentum in the form of turbulence. Describing the energy transport on the basis of the Navier-Stokes-equation (see equation (2.6)) has proven to be an irreducible problem without an analytical solution ("turbulence closure problem", see

(*Durbin and Reif*, 2011)). In the case of high Reynolds numbers (>1000), an approximate partition of the energy spectrum $E(k)$ depending on the wavenumber k can be performed. The main momentum transport happens at large scales, while the energy dissipation happens at small scales. An overview is given in figure 2.3. Energy is transferred from large to small scales by a process called "vortex stretching". The energy budget remains constant, therefore this regime is referred to as the "inertial" subrange. The spectral energy density in this range is proportional to (*Kolmogoroff*, 1941):

$$E(k) \propto \epsilon^{\frac{2}{3}} k^{-\frac{5}{3}}$$

ϵ refers to the turbulent energy dissipation rate.

At smaller scales, energy is dissipated to heat by friction. This "viscous" subrange features a spectral energy density proportional to (*Heisenberg*, 1948):

$$E(k) \propto k^{-7}$$

At large scales, bouyancy forces dominate over inertial and viscous forces. The form depends on the Brunt-Väisälä-frequency (see equation 2.5) (*Zimmerman and Murphy*, 1977):

$$E(k) \propto N^2 k^{-3}$$

The input of energy is at even larger scales, where local conditions feed the cascading turbulence but no general description can be given. It is referred to as the "energy" subrange.

The transitional wavenumbers between the inertial subrange and the buoyancy and viscous subrange defines a so-called outer and inner scale, respectively (*Tatarskii*, 1971). By determining these transition points, the relation between the energy dissipation rate ϵ, the Brunt-Väisälä-frequency N and the viscosity μ can be resolved (*Lübken*, 1993).

3 Overview of wind speed tracking methods

3.1 In-situ methods

Sensor	Technique	Parameters	Capabilities
Inflatable Sphere	• Drag acceleration and velocity calculated from precision radar track	• Temperature/ Density/ Winds • ~30-90 km	• Error: ~ 5% in winds • Day/Night • Radar required
Super-Loki Datasonde	• Temperature measured by thermister • Drag acceleration and velocity calculated from precision radar track	• Temperature/ Winds • ~20-70 km	• Error: typically ~20 m/s in winds • Day/Night • Radar required
Rigid Sphere	• Senses drag acceleration	• Temperature/ Density/ Winds • ~60-150 km	• Sensitivity: ~ 2 to 5 m/s for winds • Day/Night • Radar required
Foil Chaff	• Drag acceleration and velocity calculated from precision radar track of small thin metalized strips	• Winds • ~75-95 km	• Error: typically ~ 15 m/s in winds • Day/Night • Radar required
Chemical Release	• Photograph chemical trail movement	• Winds • ~80-200 km	• Sensitivity: ~ 5 to 10 m/s for winds • Night • Remote sites required

Table 3.1: Overview of in-situ wind sounding methods and their range and accuracy. Figure adapted from *Shah* (2009). Data based on *Schmidlin* (1986); *Müllemann* (2004); *Philbrick et al.* (1978); *Murayama et al.* (1999); *Larsen et al.* (2003)

In-situ measurements refer to the placement of probes in the atmosphere, which allow from their observation the derivation of the wind field and other local properties around them. An overview over several such probing methods including their applicable altitude range and accuracy is given in table 3.1. The 5% wind error given for the inflatable sphere corresponds to ± 3 m/s below 80 km for a typical falling sphere (shown by *Müllemann* (2004) for a falling sphere during the MIDAS/SOLSTICE campaign). The calculations in this chapter apply equally to the inflatable sphere, rigid sphere and Super-Loki datasonde, although the latter is the sounding method used in this study.

Recording the trajectory $\vec{r}(t, x, y, z)$ of a falling object enables the calculation of its velocity and drag. Taking the inertia of the sphere into account allows the deduction of local air densities, temperatures and wind speeds. In order to do that, it is necessary to solve the local equations of motion (2.4)

$$m\frac{d^2\vec{r}}{dt^2} = \vec{F_G} + \vec{F_C} + \vec{F_R}$$

The forces are gravity F_G, Coriolis force F_C, and friction F_R. The pressure gradient force F_p is omitted due to the high mass of the datasonde.

$$\vec{F_R}(\frac{d\vec{r}}{dt}, \rho, C_D) = -\frac{1}{2}A_B C_D(M_a, R_e)\rho\left|\frac{d\vec{r}}{dt} - \vec{w}\right|(\frac{d\vec{r}}{dt} - \vec{w})$$

A_B is the cross-section of the sphere, C_D the coefficient of friction, ρ the density and $\vec{w}$ the windspeed. C_D is parameterized through the Mach-number M_a and the Reynolds-number R_e, which depends on the dynamic viscosity μ, speed of sound c and sphere radius r_S.

In the subsonic regime, during which our measurements are performed, the drag coefficient C_D is assumed to be constant up to $M_a = 0.6$ according to the modified Newtonian theory for blunt bodies (*Carter et al.*, 2009).

$$M_a\Big(T, \left|\frac{d\vec{r}}{dt} - \vec{w}\right|\Big) = \frac{\left|\frac{d\vec{r}}{dt} - \vec{w}\right|}{c}$$

$$R_e\Big(\rho, T, \left|\frac{d\vec{r}}{dt} - \vec{w}\right|\Big) = \frac{2r_S\rho\left|\frac{d\vec{r}}{dt} - \vec{w}\right|}{\mu}$$

$$\vec{F_C}\Big(\frac{d\vec{r}}{dt}, \vec{\omega}\Big) = -2m(\vec{\omega} \times \frac{d\vec{r}}{dt})$$

$$\vec{F_G}(\vec{r}, \rho) = \vec{g}(\vec{r})(m - \rho V_S)$$

V_S is the volume of the sphere and $\vec{g}$ the acceleration due to gravity, which depends on the earth radius R_E, height above sea level h and gravity at sea level g_0

$$\vec{g}(\vec{r}) = -g_0\frac{R_E^2}{(R_E + h)^2}\frac{1}{R_E + h}\begin{pmatrix} x \\ y \\ z + R_E \end{pmatrix}$$

Calculating the speed and acceleration at every point of the trajectory leads to an underdetermined system of 3 equations.

3.2 Remote sensing methods

Remote sensing methods refer to the measurement of atmospheric properties from a distance to the sounding volume. Radar and lidar instruments are used in this study and two examples of a remote measurement technique.

3.2.1 Radar

The acronym “radar” stands for radio detection and ranging and is a method for remote sensing by way of detecting the radio echo returned from deflecting targets. While several functional setups exist, the Doppler method used in the Saura MF radar is most relevant to this study (*Hocking*, 1997).

For the MF radar, a large antenna is used for both transmitting and receiving radio waves. The received signal is Doppler shifted relative to the transmitted one due to the motions of the scatterers and this shift is recorded. In the case of a tracking radar, an operator aided by an automatic control loop follows the target by steering the radar beam along the trajectory, while an atmospheric radar combines the readings in the measurement volume to construct a profile of the net wind motion. Further information about the specifics of each approach can be found in sections 4.2 and 4.5.

3.2.2 Lidar

The acronym “lidar” stands for light detection and ranging and is a method for remote sensing of different physical properties by way of measuring backscattered light pulses. It is an “active” method in the sense that the instrument itself consists of two branches, an emitting Laser branch and a detecting telescope branch. The lapsed time between emission and detection of a light pulse allows the calculation of the distance to the scattering object. In our case, these objects are air molecules and aerosols suspended in the atmosphere. These targets each have different scattering cross-sections and distributions of density in the sounding volume of the laser beam. Assuming an isotropic probability distribution of the scattering direction, the amount of detected light pulses decreases quadratically with the distance from the scattering volume. Taking all these factors into account allows the construction of a density height profile (*Kent and Wright*, 1970). Further analysis of the backscattered spectrum at different wavelengths and polarization enables the distinction of scattering particles and determination of physical properties such as wind speed.

4 Experimental Setup

4.1 Suborbital rocket type

4.1.1 Meteorological sounding rockets

Sounding rockets in conjunction with falling sphere payloads ejected at the apogee have been in use since the 1950's. They are used for temperature-, density- and windspeed measurements (*Schmidlin et al.*, 1991), (*Lübken et al.*, 1994). The payload is Radar-reflective and tracked during its fall from a ground-based radar station. The effective range of measurements is $\approx 30-95$ km, depending on the apparatus and the scientific objective. Low atmospheric density in the upper mesosphere leads to a small drag force opposite the rocket trajectory and consequently high speeds of the payload imparted by the impulse of the rocket movement. This movement normalizes with lowering altitude and increasing density, and from ≈ 70 km onward we assume the falling sphere's movement is independent from the launch trajectory. At the lower end of the altitude range below 30 km, the air pressure from the surrounding atmosphere in combination with the stress of a rocket launch on the balloon membrane leads to a puncture of the hull and the collapse of the balloon, although this scenario can also occur at higher altitudes due to malfunction.

4.1.2 Super-Loki chassis details

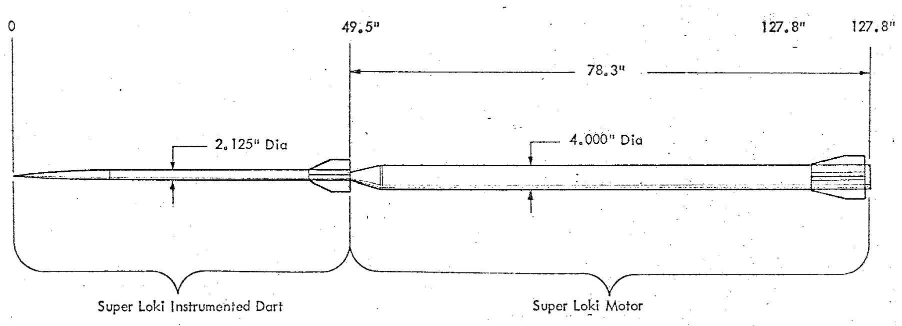

Figure 4.1: Diagram of an assembled Super Loki Instrumented Dart and Motor. The motor has a length of 1.98 m, a diameter of 10.2 cm and features a loaded mass of 22.3 kg. The dart has a length of 1.26 m, a diameter of 5.4 cm and a weight of 6.35 kg (*Space Data Corporation*, 1998).

The Super Loki solid propellant rocket motor is used for sub-orbital sounding rocket applications since April 1968. It is a successor of the two-stage Loki design with a burn time of 2 s in order to reach higher altitudes (up to 85 km) with a payload. The payload is attached in the form of an inert dart with a high ballistic coefficient. To improve the trajectory of the Superloki motor after burn-out and prevent impact on habitated areas additional balance weight of about 200 g was added in the front of the motor. The rocket configuration is shown in figure 4.1.

4.2 Radar tracking apparatus

Figure 4.2: RIR-774C C-Band Tracking radar at Andøya Rocket Range, Norway (*Altenbuchner et al.*, 2012). The paraboloid tracking antenna is located on top of a 20 ft container (≈ 6 m).

4.2.1 Tracking properties of the RIR-774C

The payload trajectory has been recorded using the RIR-774C Tracking radar operated by DLR-MORABA (*Kalteis*, 1993). A picture of the Tracking radar with the fast steerable antenna is shown in figure 4.2. It radiates in the C-Band at 5600 MHz using the so called monopulse-technique, which uses the backscattered target signal to correct the beam guidance. The error is +/- 5 m in the range coordinate and +/- 0.015° in the angular coordinates. The pulse frequency is 640 Hz and the pulse width 0.5 s. The measurements are not independent due to the beam guidance lag of 0.3 s. The data is recorded with 50 Hz and smoothed with a Hanning-Filter in the subsequent processing to reduce noise and enable first- and second-order derivation.

4.2.2 Accuracy

Taking the rocket configuration (see section 4.1.2) into account, it follows that at a payload altitude of $\approx 70 - 80$ km and a horizontal distance of 50 km, the error range of the recorded data is about 10 m. Unfortunately, the payload containers or parts of a disintegrating payload are capable of confusing the radar system below 80 km, raising the error range to +/- 50 m (e.g. *Becker* (1995)).

4.3 Datasonde

Figure 4.3: Picture of a starute payload inflated at Michigan Tech University. It has a diameter of 2.13 m and a weight of 0.155 kg (*Suits*, 2014).

4.3.1 Properties

The passive payloads during the meteorological rocket launches of the WADIS campaign are part of the 11D datasonde Dart (OSC P/N 395-810), manufactured by the Orbital Launch Systems Group specifically for the Super Loki motor. They were originally designed to transmit in-situ temperature data sensed by a thermistor to a ground reception system, in addition to a radar system tracking the position. That capability contributes to the weight of 0.5 kg of the payload and consequently to a lower apogee of the flight compared to a falling sphere probe. Temperature sensors were not evaluated during the campaign, but were kept on the payload to stabilize the starute (stable retardation parachute, see figure 4.3) during the fall. The age of the rockets of approximately 20 years led to doubts about the reliability of the NiCd battery components inside the payload. The majority of launches were successful, with strictly passive radar tracking of the payload attached to a Mylar starute. The ejection was pyrotechnically performed at an apogee between 70 km and 78 km. The fall speed of the starute was about 85 m/s at 60 km.

4.3.2 Drag correction

Continuing from section 3.1, it is necessary to introduce a number of simplifications in order to reduce the number of free variables in the equation system. The datasonde in our measurements functions as a non-spherical larger and heavier version of a falling sphere (*Philbrick et al.*, 1985). We assume the gravitational acceleration is not dependent on height $g(z) = g_0$ and that vertical winds are zero: $w_z = 0$. Further, we disregard the Coriolis force $F_C = 0$ due to the low trajectory distance. The buoyancy of the starute $F_B = -g\rho V_S$ can also be neglected due to the payload weight. Performing the substitution

$$\left|\frac{d\vec{r}}{dt} - \vec{w}\right| = \sqrt{u_r^2 + v_r^2 + w_r^2}$$

in which u_r, v_r, w_r denote the relative wind speed to the datasonde, we obtain the following expression for the drag force (*Eddy et al.*, 1965):

$$\vec{F_R} = \frac{1}{2} A_B C_D \rho \sqrt{u_r^2 + v_r^2 + w_r^2} (\vec{e_x} u_r + \vec{e_y} v_r + \vec{e_z} w_r)$$

The equation of motion of the starute is calculated analogously to a packet of air in section 2.5. Summing over the impacting forces in equation (2.4) and expressing the acceleration in components with $K = \frac{1}{2} A_B C_D \rho$ gives the equation system

$$m \frac{d^2 r_x}{dt^2} = u_r K \sqrt{u_r^2 + v_r^2 + w_r^2}$$

$$m \frac{d^2 r_y}{dt^2} = v_r K \sqrt{u_r^2 + v_r^2 + w_r^2}$$

$$m \frac{d^2 r_z}{dt^2} = -g + w_r K \sqrt{u_r^2 + v_r^2 + w_r^2}$$

The wind speed of the surrounding volume of the datasonde w_x, w_y, w_z is the physical condition we are interested in. This background wind is sounded through the intermediary of the movement of a tracer in the form of the datasonde. Eliminating w_r from the equation system above leads to an expression for $w_x = \frac{dr_x}{dt} - u_r$ and $w_y = \frac{dr_y}{dt} - v_r$, the zonal and meridional wind, that can be easily evaluated using finite difference calculus from the datasonde trajectory (*Eddy et al.*, 1965):

$$w_x = \frac{dr_x}{dt} - (\frac{dr_z}{dt} \frac{d^2 r_x}{dt^2}) / (\frac{d^2 r_z}{dt^2} + g)$$

$$w_y = \frac{dr_y}{dt} - (\frac{dr_z}{dt} \frac{d^2 r_y}{dt^2}) / (\frac{d^2 r_z}{dt^2} + g)$$

Notably, these equations do not depend on the mass of the datasonde or its volume (*Eddy et al.*, 1965).

4.4 ALOMAR RMR-Lidar

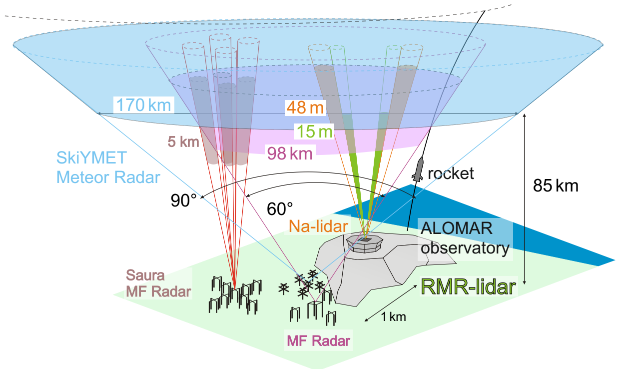

Figure 4.4: Sounding volumes of the different instruments at ALOMAR. RMR-Lidar in green and Saura MF radar in red, with the sounding diameter in 85 km annotated and the actual sounding volume filled solid (modified after *Hildebrand* (2014)).

4.4.1 Overview of instrument setup

The ALOMAR RMR-Lidar is located at the ALOMAR research station in northern Norway (69°N, 16° E). At this station several remote sensing instruments allow to study the thermal and dynamical structure of the middle atmosphere. An overview of different wind measurement techniques is shown in figure features 4.4. At the ALOMAR station, two Nd:YAG power lasers emit pulsed laser beams and two telescopes register the backscatter from the atmosphere. A single time-sliced photon detection system is utilized for both. The pulses are $\approx$ 10 ns long, emitted along the optical axis of the telescopes at 30 Hz and contain 3 wavelengths: 1064 nm, 532 nm and 355 nm. Only light at 532 nm is used in the DoRIS measurements. The laser beam is widened to a 20 cm diameter in order to attain a beam divergence $\lesssim$ 70 µrad (*Hildebrand*, 2014).

The acronym RMR stands for Rayleigh/Mie/Raman scattering and describes the ways that emitted light can interact with a particle. Rayleigh and Mie scattering are analogous to elastic collisions with a particle much smaller than the wavelength of a photon (Rayleigh) or on the same scale (Mie). Raman scattering leads to a characteristic wavelength shift in respect to the incoming radiation and is not elastic. The RMR lidar instrument at ALOMAR is capable of processing each type of interaction for a comprehensive analysis of the composition of the atmosphere (*Baumgarten*, 2010).

The receiving telescopes have a diameter of 1.8 m, a focal length of 8.3 m and a field of view of 120 µrad (*Grzegorzewski*, 2013). They can be tilted off-zenith up to 30° and feature a Cassegrain design. The capability of an off-zenith viewing geometry is essential to measure horizontal wind components as only the line-of-sight air motions lead to a Doppler shift of the backscattered light. Backscattered light of each telescope is integrated over 1000 emitted pulses ($\approx$ 33 s) and sorted into range bins of 50 m using different detector ranges ranges: 70 - 44 km, 44 - 27 km and below 27 km.

4.4.2 DoRIS wind retrieval

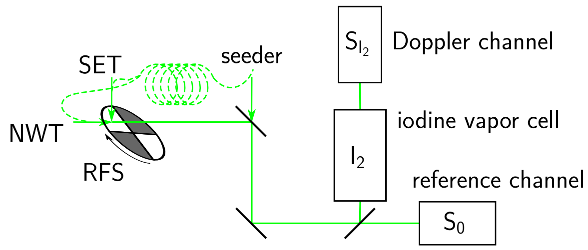

Figure 4.5: Basic setup of the DoRIS instrument: The signal from the SET and NWT telescopes is alternately fed into the detection channel, where the ratio between the original signal (S_0, reference channel) and the iodine filtered signal (S_{I_2}, Doppler channel) is a measure of the Doppler shift and hence, wind speed (*Hildebrand et al.*, 2012).

DoRIS stands for "Doppler Rayleigh Iodine Spectrometer" and is the instrument at ALOMAR allowing the retrieval of wind speed profiles reaching up to the upper mesosphere. The backscattered light pulses display a shift in wavelength according to the Doppler effect caused by moving scattering centers. This shift is detectable using a cell of molecular iodine with an absoption line at the frequency of the laser line. A schematic of the detection system is shown in figure 4.5. In practice it is necessary to measure temperature concurrently because of a temperature sensitive broadening of the incoming spectrum. Excluded are altitude ranges with a significant aerosol concentration, because the higher specific mass of the aerosol particles requires too precise calibration depending on the partial pressure (*Baumgarten*, 2010). The lidar data presented in this study has been pre-processed by Jens Hildebrand and Gerd Baumgarten.

4.4.3 Daylight filter

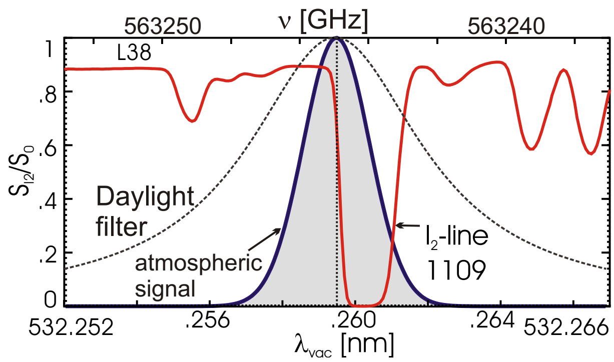

Figure 4.6: Spectral profile of the daylight filter superimposed on the I_2-spectrum in the DoRIS and an example of the Cabannes line (*Baumgarten*, 2014).

The rocket and lidar measurements have been performed in June 2013, so during polar daytime conditions. Daytime operations present significant challenges on lidar soundings. An additional spectral filter in the receiving branch of DoRIS is employed to seperate the solar background radiation from the wavelengths of the backscattered laser light. The emitted light has a frequency variability of 50 MHz, in addition air motions induce a Doppler shift of 3.75 MHz / (m/s), necessitating a wider spectrum range of the filter beyond the Cabannes-line. Details of the spectral characteristic of the relevant components of DoRIS are show in figure 4.6. This increases the number of false positives and decreases the count rate of scattered photons (see 6.1.1)

4.5 Saura MF radar

The physical principle of the MF radar located at Saura is to examine irregularities in the refraction index of the ionosphere. When radio waves are partially reflected by charged particles such as electrons in the atmosphere, it is possible to measure the wind in the upper mesosphere by employing a Doppler method similar to the one described in section 3.2.

The Saura MF radar, located near the Andøya Rocket Range with a diameter of about 1 km, is capable of directing the radar beam in 8 directions at 2 azimuthal angles with an altitude range of 50 - 94 km. This flexibility makes it uniquely suited to compare the wind data to the other retrieval methods. It features a vertical resolution of 1 km and a temporal resolution of 30 min at a frequency of 3.17 MHz (*Singer et al.*, 2003).

5 Rocket Methodology and Measurements

5.1 WADIS campaign

Figure 5.1: Andøya Rocket Range near Andenes, Norway (*MM2sp*, 2014)

The first rocket campaign as part of the WADIS (Wellen, Ausbreitung und Dissipation in der Mittleren Atmosphäre[1]) research project at the Andøya Rocket Range in Norway[2] consisted of 1 launch of an instrumented sounding rocket and 11 launches of smaller meteorological rockets carrying datasonde payloads. The launches in the time period of June 26. - July 1. 2013 from the Andøya Rocket Range (figure 5.1) were accompanied by concurrent ground-based Lidar- and Radar-measurements.

The research objective of both the first campaign during the polar summer and a future campaign in the winter months is to observe gravity wave propagation from its excitation in the troposphere to its dissipation in the upper mesosphere. This study is focused on the intercomparison of ground-based lidar wind profile measurements using the ALOMAR RMR-Lidar with in-situ wind measurements using a falling datasonde. Each method's accuracy and significance when identifying gravity waves is evaluated.

5.1.1 Launch overview and lidar measurement duration

The specifics of the Superloki launches during the WADIS campaign can be seen in table 5.1. The launches were performed during polar summer mostly at clear tropospheric day time conditions in the evening hours.

[1]waves, propagation and dissipation in the middle atmosphere
[2]69°N 16°E

All 11 meteorological rockets successfully reached the target altitude between 70 and 80 km at an azimuthal launch angle of 330° and an elevation angle of 81°, but two payloads failed to eject during launch 4 and launch 10. As a consequence there is no data for these launches, the original launch numbers continue to be used further in this study. In addition, the datasonde payload during launches 2, 3 and 11 disintegrated above 30 km, thereby limiting the useful data range. The radar track has been lost during the ascent of rocket launches 1, 5 and 6, before being regained during the descent of the datasonde, hence the true apogee is unknown. In the case of launch 3, it was possible to track a part of the debris down to an altitude of 20 km. The breakup occured at approximately 63 km altitude. An example of the debris is shown in figure 5.2. Due to the debris, the trajectory data is unreliable down to an altitude of about 50 km. Below that mark, the spatial separation of the debris was large enough to allow the tracking of a single piece. Since the formula used for drag reduction (section 4.3.2) is independent of the mass of the probe, the results of the wind calculation should still be valid. While the lidar measurements were conducted simultaneously during all the launches except for launch 1, the comparison between the methods will concentrate on the launch series of the 30.06. / 01.07., in which 6 rockets were launched in the span of 3.5 h. Of those 6 launches, 5 (launches 5, 6, 7, 8 and 9) completed soundings from $\approx 75 - 25$ km with a good temporal resolution due to an overlap of the descent timeframes (≈ 40 min until 30 km) of the Datasondes. Initially two lidar telescopes at ALOMAR were aiming in the launch direction of 315° azimuthal and 30° elevation angle (NWT) and the zonal direction of 90° azimuthal and 20° elevation angle (SET). The NWT azimuth was chosen to be 315° after the analysis of the first two datasondes. This minimized the distance to the lidar beam. Details of the rocket launches are in table 5.1.

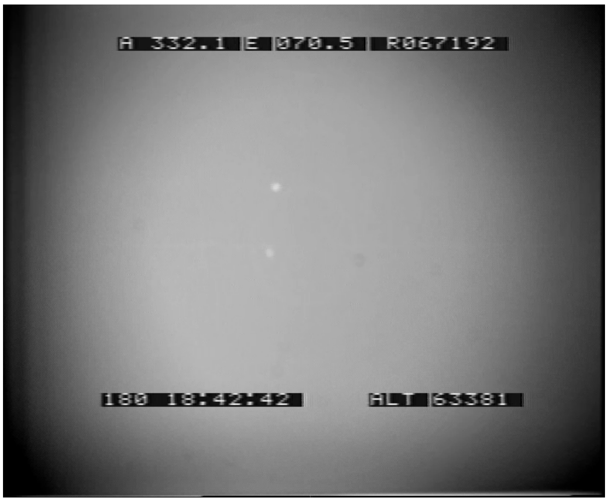

Figure 5.2: Picture taken by a guiding camera coaligned to the beam of the RIR-774C tracking radar. Two bright spots in the image center indicate the disintegration of the starute during launch 3. Trajectory information (azimuth, elevation, range) is given by the numbers on the top of the picture. Time and altitude is given in the bottom.

launch number	date	launch time [UTC]	apogee [km]	lowest track. [km]	70 km timest. [s]	30 km timest. [s]	horiz. distance [km]	NWT azim.
1	26.06.13	23:08:00		19.63	148	1332	26.49	330
2	27.06.13	21:55:00	69.98	52.76	107		17.63	330
3	29.06.13	18:39:00	74.57	21.76	147	2544	50.77	315
4	30.06.13	21:31:00						315
5	30.06.13	22:34:30		22.79	147	1315	24.67	315
6	30.06.13	23:20:00		29.60	121	1361	19.61	315
7	30.06.13	23:51:00	78.03	26.41	176	1362	23.64	315
8	01.07.13	00:30:00	75.68	29.68	159	1349	22.77	315
9	01.07.13	01:03:00	74.89	17.66	158	1320	29.06	315
10	01.07.13	18:53:00						315
11	01.07.13	19:30:00	78.15	33.38	173		14.61	315

Table 5.1: Overview of meteorological rocket launches during the WADIS campaign. The apogee of the rocket is given if confirmed by the radar operator, while the lowest track refers to the lowest valid altitude data from the radar, at which the projected distance on the earth surface from the radar station to the datasonde has been calculated as the horizontal distance. The timestamp refers to the elapsed time after rocket launch at a specific altitude in s.

5.1.2 Datasonde trajectories

The datasonde payloads descended from the apogee between 70 and 80 km in the westward direction for the entire 5-day campaign duration (see figure 5.3). During their descent, a lateral distance of ≈15-30 km from the launch site is typically covered before the implosion of the starute above the Atlantic ocean, well within the parameters of the margin of error given in section 4.2.2. The exception of the comparatively long travel distance of launch 3 is explained with the lower mass and higher drag of the debris that has been tracked from 50 km down to an altitude comparable with the other successful datasonde soundings. This corresponds to a slower descent time at 76 min relative to a typical time of ≈ 45 min. The additional source of error due to the lateral extension of the sounding is disregarded, as the unreliability of the data between 50 km and 70 km makes the wind data unsuitable for further analysis. The temporal extension of the datasonde sounding can influence the analysis in line with the atmospheric variability of the launch conditions. To minimise the impact, several measurements in a close timeframe are necessary, which justifies the focus on the launches during the 30.06./01.07.2013.

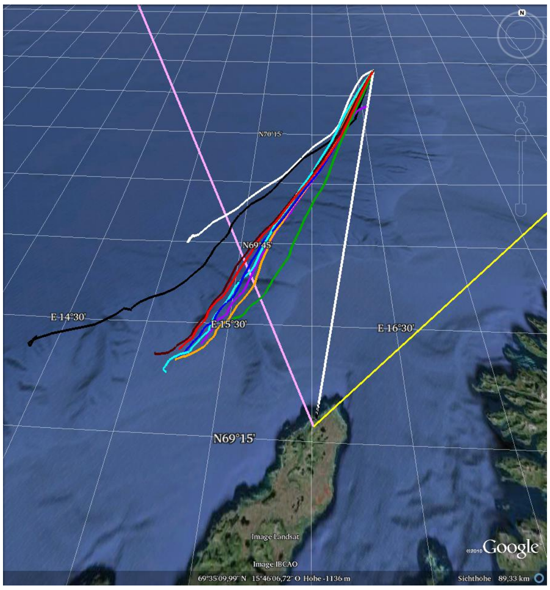

Figure 5.3: 3D visualization of the datasonde trajectories below 70 km altitude and the lidar pointing direction (launch 5: blue, launch 6: green, launch 7: violet, launch 8: red, launch 9: cyan, all other launches in black, NWT lidar: pink, SET lidar: yellow - Source: "Andøya." 69°49'20,73" N and 15°51'35,44" E. **Google Earth**. 2010. 10.04.2014)

The lidar telescopes aim 15° off the launch direction (NWT: 315° AZ, 30° EL) and in the zonal direction (SET: 90° AZ, 20° EL) during the rocket soundings after the test launches 1 and 2. In order to evaluate the agreement of the wind measurements of both instruments, it is useful to evaluate their spatial relationship to the datasonde soundings. While the SET lidar beam points away from the westward trajectory along the circle of latitude with a minimum distance from the datasonde of ≈ 20 km at 50 km altitude, the NWT lidar beam direction has been chosen to approach the datasonde trajectory as closely as possible. The distance between the NWT lidar beam and the datasonde trajectory is calculated separately in both the zonal and meridional direction, with the square root of the sum of squares indicating an upper bound on their distance in 3D space. As can be seen in Figure 5.4, the closest common sounding volume is at an altitude of ≈ 54 km, with launch 5 coming nearest to the NWT lidar beam within ≈ 0.5 km (see table 6.1).

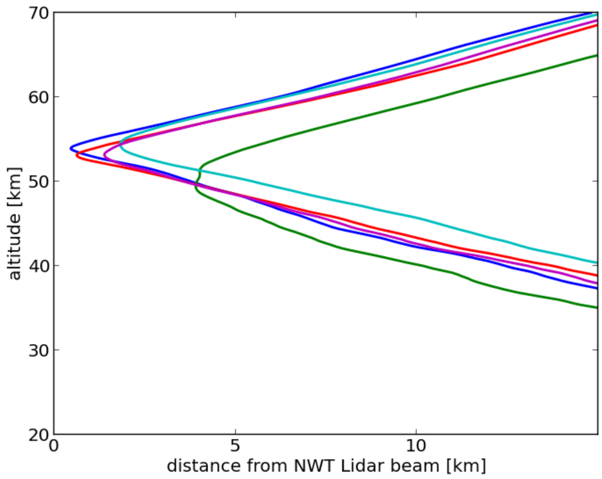

Figure 5.4: Distances of the datasonde from the NWT lidar beam for the launches 5 (blue), 6 (green), 7 (violet), 8 (red) and 9 (cyan)

5.1.3 Analysis algorithm and software

The datasonde trajectory tracked by a ground-based radar station (see 3.2) with a 50 Hz data rate is insufficient by itself for a comparison to lidar wind data. A new analysis software has been written in the python language to process the raw data. It follows a number of pre-processing steps and filters the data recorded according to the following criteria:

1. From the raw radar data only the data points are considered, which are marked as “on target” by the radar operator. The first “on target” data point receives the time stamp 0.
2. The highest altitude value in the data is considered the apogee, and all data previous to its time stamp is regarded as part of the rocket trajectory and discarded.

3. The radar ground system location is offset by 516 m in the zonal direction and 1649 m in the meridional direction from the ALOMAR RMR-Lidar. In order to align the origins of both coordinate systems, the radar data is shifted by the same amount.
4. The trajectory data is smoothed using a Hanning-filter with a window size of 1 s[3] in order to reduce the noise introduced by the radar tracking and allow further first- and second order derivation of the continous trajectory using finite differences (*Harris*, 1978).
5. The radar data is sampled with a constant rate relative to time, which means a higher positional resolution in the lower altitude range than in the higher altitude range due to the decelerating datasonde. In the further analysis, an even sampling along the height coordinate is desired to calculate the horizontal wind profiles with an even resolution. This is achieved using a 3D spline fitted exactly along the smoothed coordinates and evaluated again with a 100 m vertical resolution.
6. The error bars in the wind profiles are estimated using the standard deviation of the original data points before the spline fit inside the 100 m vertical intervals, divided by the time lapsed during the traversal of the datasonde inside the interval.
7. The horizontal velocity of the datasonde is calculated by dividing the gradient of the positional data with the gradient of the time stamp data, and the acceleration in turn by dividing the gradient of the velocity with the gradient of the time stamp data again. Vertical wind data is not considered in this study. The calculations are discrete using finite differences with the vertical 50 m resolution data. The datasonde serves as a probe for the background wind, which means a drag correction needs to be performed to account for its inertia. The method is explained in section 4.3.2.
8. The datasonde velocity is evaluated in the zonal and meridional direction during its descent along the trajectory, while the NWT lidar beam points in a direction close to the datasonde around an altitude of 50 km. In order to compare both, the wind speed components are projected along the azimuthal direction of the NWT lidar beam. Because the SET lidar beam points in the zonal direction, it is compared to the zonal component data of the datasonde. These instruments do not cover the same sounding volume, so local variations in wind speed are possible along their parallel orientation.

5.2 Wind profiles of the datasonde soundings

The results of the processing in 5.1.3 for launch 8 are shown in figure 5.5. The individual results of all launches are found in the appendix figures 8.6, 8.7 and 8.8. Common to all wind profiles are a large amount of noise above 60 km, indicating an erroneous computation of the wind speed due to the low vertical resolution and high noise of the radar at these altitudes, when tracking false positives such as debris of the rocket. The noise

[3]FWHM 0.5 s

normalizes below 50 km and follows the wind model data made available by the European Centre for Medium-Range Weather Forecasts (ECMWF) remarkably well (*Molteni et al.*, 1996). The ECMWF profiles are available every 6 h, so there is not generally a profile concurrent to a given launch available, yet even the next timeliest profile appears to follow the wind dynamics with the exception of wind peaks with a vertical width < 1 km. The spread of wind velocities around the ECMWF profile decreases with altitude, although an upper bound can be set at ± 10 m/s in the zonal and meridional direction.

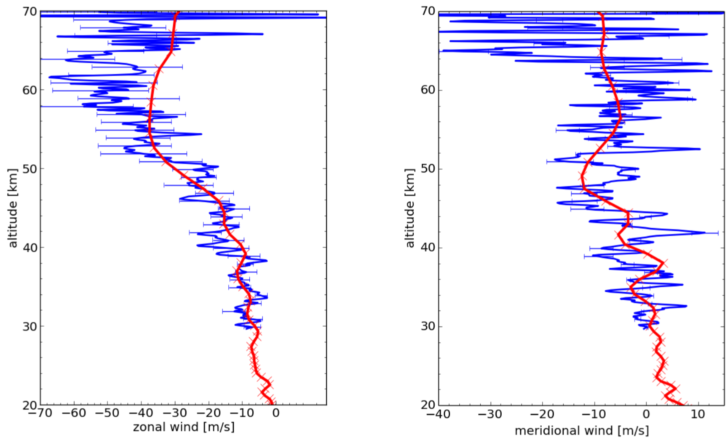

Figure 5.5: Wind profile of meteorological rocket launch 8 in blue. For comparison, the ECMWF data of the 01.07.2013 at 0 UT has been added in red. Blue horizontal bars indicate the uncertainty of the measurements as discussed in section 5.1.3.

Mesurements have been performed during summer conditions, for which the typical westward and southward flow has been observed (see figure 2.2). The zonal wind speed in the used HMW07 model ranges from -50 m/s in the mesosphere to 0 m/s in the lower stratosphere, while the meridional wind speed ranges from -20 m/s to 20 m/s in the mesosphere to -10 m/s to 10 m/s in the stratosphere. The measurements were all conducted in the subsonic flow regime with Mach numbers ranging from 0.35 to 0.6 (see 3.1).

The mean profile shown in figure 5.6 is in good agreement with the ECMWF data at 0 UT. A significant deviation is found in the zonal profile between 52 km and 40 km, where a wind shear slows down the westward wind above 44 km and accelerates it below 44 km. At 60 km altitude, as the wind speeds increase to 20 m/s ahead of the expected profile, the large variation in speeds at these altitudes makes an evaluation unreliable.

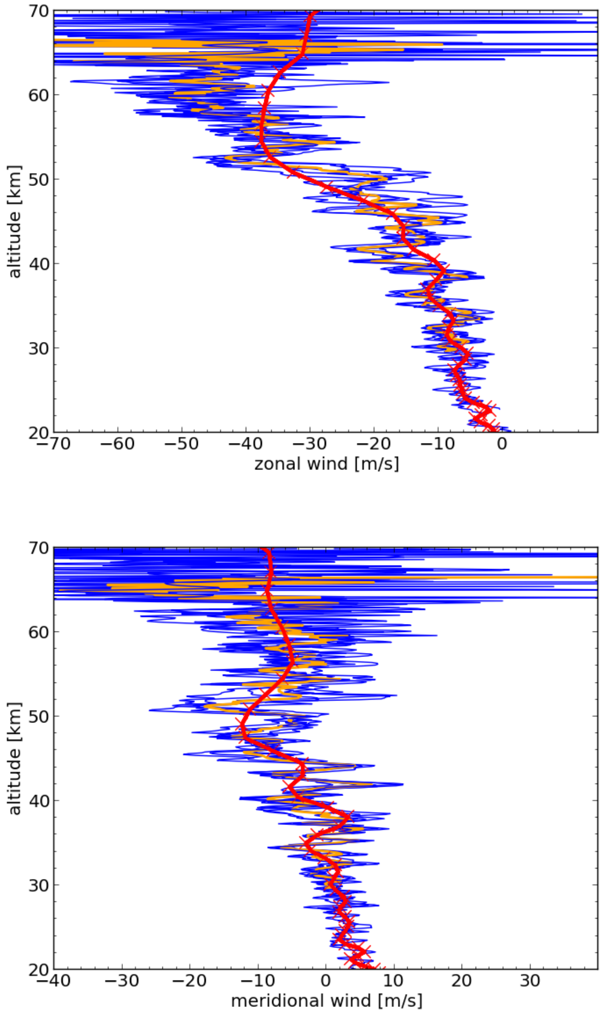

Figure 5.6: Common plot of the launches 5, 6, 7, 8 and 9, which occurred in a 2.5 h window. The mean profile of the launches is shown in orange. For comparison, the ECMWF data of the 01.07.2013 at 0 UT has been added in red.

The time-spaced wind profiles shown in figure 5.7 allow the tracing of possible wavelike phase structures in the wind data. Gravity waves increase in wavelength with altitude, so it should be possible to observe this behavior if they appear (*Schöch*, 2007). It should be noted that the errorbars in the zonal diagram are larger than in the meridional case because of the movement of the datasonde in the approximate zonal direction.

In the 2.5 h timespan of the observation, no significant phase movement appears. A weak zonal wind gradient and a large error range renders wave detection inconclusive.

In the meridional case, a wind shearing splits at 44 km and is followed by two distinct peaks in the eastward direction. Its origin is independent of the expected origin of gravity waves in the troposphere.

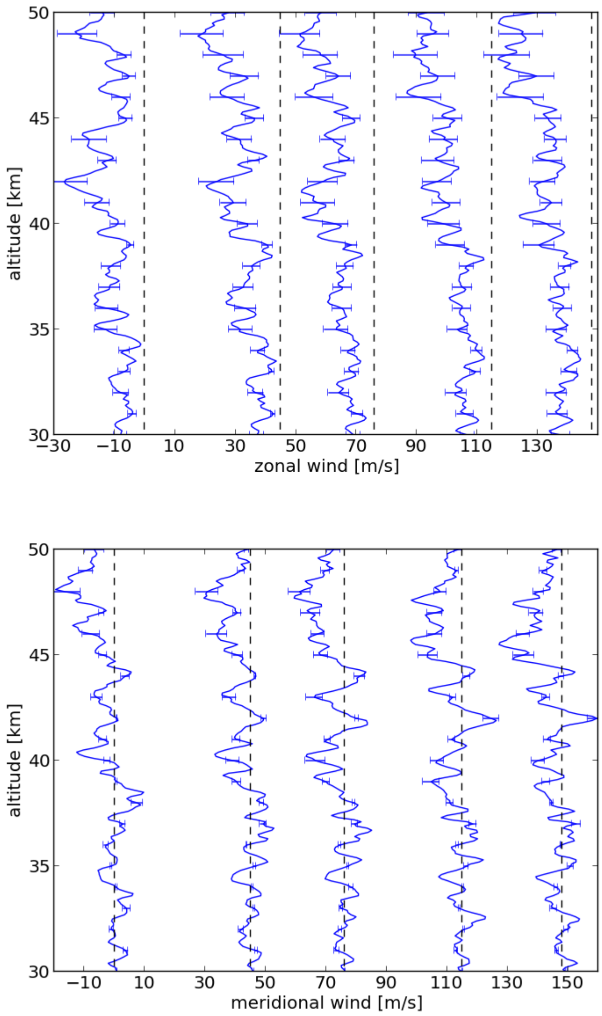

Figure 5.7: Common plot of the launches 5, 6, 7, 8 and 9, which occurred in a 2.5 h window. The wind axis is correct for the first profile from the left, while each successive profile is shifted by +1 along the x-axis per minute time difference. The dashed line represents the origin relative to the profile.

5.3 Error discussion

5.3.1 Original datasonde analysis approach using the ROBIN program

The original analysis approach was to use the HIROBIN program, which is an expanded version of the ROBIN program written in the early 1960's intended for the ROBIN[4] falling sphere (*Engler*, 1965). While the application has been continuously extended and temperature and wind measurements refined, only the differentiation and drag correction of the datasonde trajectory was intended to be used (*Becker*, 1995), (*Wong*, 1998). This required a number of changes to the original FORTRAN code, which might be useful in a future study:

Until the WADIS rocket campaign, the original binary compiled with the DOS WATCOM compiler from 1993 has been in use[5] for the falling sphere analysis. Many variables specific to the launch conditions, such as the weight of the probe, are set at compile time, meaning bugs in the code would be difficult to isolate in a timely manner and software availability would progressively deteriorate. In order to improve the maintainability of the program, it has been ported to Linux using the gfortran[6] compiler. Unfortunately, it had only been used until this point at a maximum data rate of 10 Hz. While a higher data rate can be set, a number of issues led to error messages at runtime, such as inconsistent timesteps and faulty acceleration profiles. Sampling the input at 10 Hz inside the program was an option, but even then dubious unphysical oscillations in the velocity data above 55 km manifested in the output (see figure 5.10). The data is of course pre-filtered to reduce noise from the Radar-tracking, which is controlled through parameters in the source code and possibly responsible for this unexpected behaviour. While some investigation has been performed, in the end it has been deemed most practical to reimplement the wind analysis in python using the drag reduction from *Eddy et al.* (1965). The new approach could be considered more direct, because the HIROBIN fortran code contains many assumptions about falling sphere behaviour which simplify the computation on magnetic tape, for which it was originally designed. In addition, the improved resolution of the source radar data allows for an improvement in the quality of the error estimation (see section 5.1.3).

5.3.2 Datasonde drag correction accuracy

In section 3.1, we assumed a constant drag coefficient C_d due to our measurements in the subsonic regime between $M_a = 0.35 - 0.6$. This assumption is central to our drag correction algorithm 5.1.3, which uses vertical acceleration to compensate for the momentum of the datasonde in the wind analysis. This assumption is not necessarily accurate, however. In the study by *Carter et al.* (2009), it is shown that C_d follows a quadratic depency on M_a in the subsonic regime, and is underestimated by the modified Newtonian theory. In addition, the necessity for drag correction decreases with decreasing altitude, as can be seen in figure 5.8. Below $\approx$ 55 km, virtually no drag correction of the datasonde winds occurs. The wind calculation algorithm (see section 5.1.3) performs identically even without taking the momentum and weight of the payload through its acceleration

[4] "Rocket balloon instrument"
[5] http://www.openwatcom.org/
[6] http://gcc.gnu.org/fortran/

into account. The conclusion of this result is that in the range of 30 to 50 km a datasonde is less inert than a faster falling sphere and drag correction therefore less necessary. The results also show that the drag correction can be a significant source of error in the altitude ranges above 50 km. A slower falling speed of 85 m/s compared to > 100 m/s at 60 km for a falling sphere renders the analysis far more sensitive to positional radar uncertainty (*Leviton and Wright*, 1961). While a traditional falling sphere has an error range of 6 m/s below 80 km (see section 3.1), the datasonde uncertainty is about 10 m/s (see table 6.2) below 60 km (*Schmidlin*, 1986). The error range reaches above 20 m/s at 66 km altitude, in excess of the range given for datasonde winds in table 3.1. After considering the possibility of error due to a flawed derivation of acceleration from discontinous trajectory data of the starute, an attempt has been made to use the continous spline representation of the trajectory to calculate winds and acceleration. Unfortunately, the results were even less physically plausible and the original finite difference calculation remained the preferred approach.

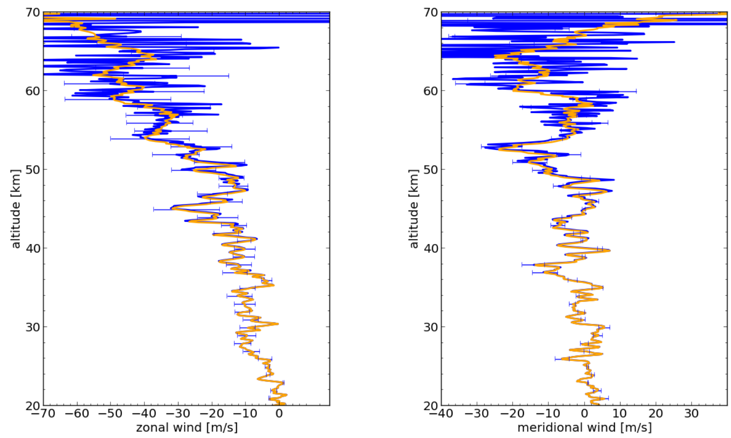

Figure 5.8: Comparison of wind profile of launch 1 before (orange) and after (blue) drag correction using the method presented in section 4.3.2

In order to independently verify the analysis, the raw radar tracking data for the first launch has been shared with Schmidlin et al. They used the ROBIN software package to generate wind profiles which appear to very closely match the uncorrected profile generated through trajectory differentiation. Figure 5.9 shows a comparison of the wind analysis described earlier to the Schmidlin results. It is important to note that the original wind speed data from Schmidlin et al. deviated from the data in this study by a factor of 5. Through private communication, an error in the configured data rate of the ROBIN program (10 Hz instead of 50 Hz) has been found and taken into account in the figure 5.9.

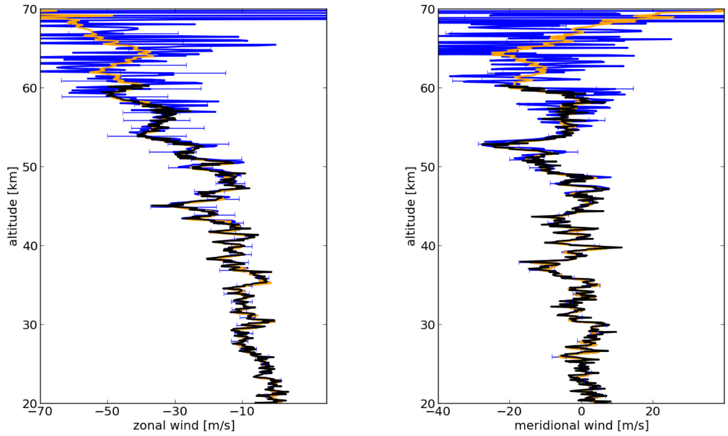

Figure 5.9: Comparison of wind profile of launch 1 before (orange) and after (blue) drag correction using the method presented in section 4.3.2 and ROBIN analysis by Schmidlin et al. (black)

Originally, use of the ROBIN program was also intended for analysis in this study. The resultant data for launch 1 is given as an example in figure 5.10. The large oscillations above 55 km appear unphysical, leading to an examination of the processing steps inside the package. Data was fed into it with a 50 Hz rate and configured to only consider every tenth data point. These values were arrived at after some experimentation to avoid runtime errors caused by unexpected data values at different points in the raw input stream, and the sampling time of 0.1 s differs from the recommended sampling time of 0.3 s between data points. It might well be that a 10 Hz rate with every 3. data point considered, as it was originally setup, runs more stable, or that additional exception handling and filtering in the FORTRAN code could diminish the breaks in the analysis.

Apart from the problems in the numerical calculation, the fact that the ROBIN program was originally designed for falling sphere measurements could be responsible for the close match of the Schmidlin et al. analysis with the uncorrected positional gradient of the datasonde. The corrections due to assumptions about falling sphere movements such as the higher falling speed might simply not apply to datasondes. Instead of attempting to further alter the program or modify the raw input to conform to constraints in the processing, the decision was made to use the positional gradient together with a drag corrected probe acceleration.

The comparisons of the different analysis shows that below 60 km no significant differences between the different methods was observed. For example the mean difference of the Schmidlin et al. ROBIN analysis of the zonal wind to our method without drag correction between 50 km and 60.5 km is 0.2 m/s, while it is 0.6 m/s with drag correction.

The difficulties in the wind analysis above 60 km in addition to the sampling inaccuracies shown in section 5.4 lead to the suggestion of a modified analysis in the future.

Separating the wind data into two or more altitude ranges with different processing parameters for each should lead to accuracy improvements in future datasonde studies.

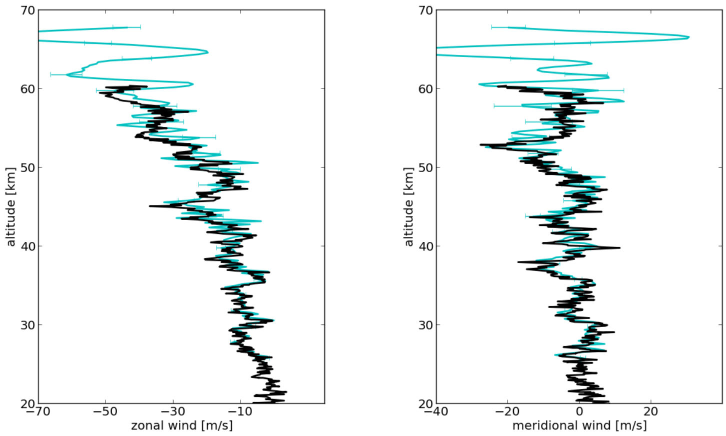

Figure 5.10: Comparison of ROBIN analysis by the author (cyan) and ROBIN analysis by Schmidlin et al. (black) of launch 1. The error bars are internal estimates of the program (*Becker*, 1995)

5.4 Comparison to ideal power spectrum

The power spectral density distribution of the datasonde wind data has been calculated using Welch's average periodogram method in the stratospheric regime between 30 and 50 km (*Bendat and Piersol*, 2011). Comparing the measured spectrum to the expected power spectrum (see section 2.7) allows to estimate the scales resolved by the datasonde. From the dynamics of the atmosphere we expect that the spectral power decays for shorter scales. On the other hand an imperfect instrument would deliver a constant power for shorter scales. The 20 km period has been chosen due to the lower noise in the source data. A slope of k^{-3} in the buyoancy subrange between 2 km and 0.2 km is expected, while a slope of $k^{-\frac{5}{3}}$ shows inertial propagation in the subrange below (see section 2.7), where k is the vertical scale considered. The energy dropoff towards small scales in the viscous subrange below scales of 0.01 km is not resolved in this analysis.

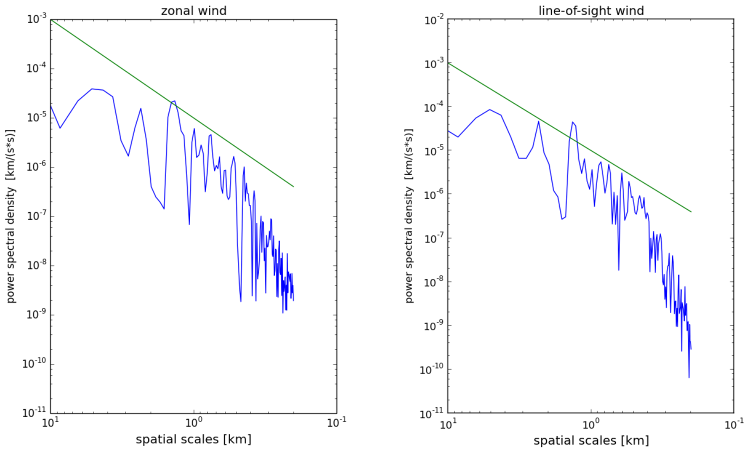

Figure 5.11: Vertical power spectral density distribution of the wind profile of launch 8 between 30 and 50 km. The mean wind inside the height interval has been substracted. An arbitrary line with a slope of $k^{-\frac{5}{3}}$ has been added in green.

Figure 5.11 for launch 8 shows a dropoff in the inertial subrange in conflict with the theoretical model, as well as a proportionality to $k^{-\frac{5}{3}}$ well into the buoyancy subrange. Two variable parameters in the analysis can influence the result of these spectra: the positional smoothing of the source radar data, which is necessary for the calculation of continuous first and second order derivations, and the sampling nodes of the horizontal wind spline, which possibly influence the resolved dynamics in the spectral distribution (see section 5.1.3). In order to account for these influences, the $\propto k^{-\frac{5}{3}}$ relationship at scales below the buoyancy subrange has been chosen as a benchmark to optimize the data analysis against. While this analysis has been performed for the zonal wind data set of launch 8, the results should apply to all power spectrum distributions due to the similar analysis steps. The temporal filtering of our source positional data (see section 5.1.3) has a dampening effect on the reproduction of the high frequency power spectrum, as can be seen in figure 5.12. The very lightly filtered spectrum in blue (a 0.06 s window corresponds to 3 data points) is closely tracked by the spectrum at a filter value of ≈ 1 s. Even a filtering value 4 times as high has only a modest impact on the energy amplitude $E(k)$ at high frequencies. Due to its limited impact, the value of 1.06 has been chosen in the subsequent analysis.

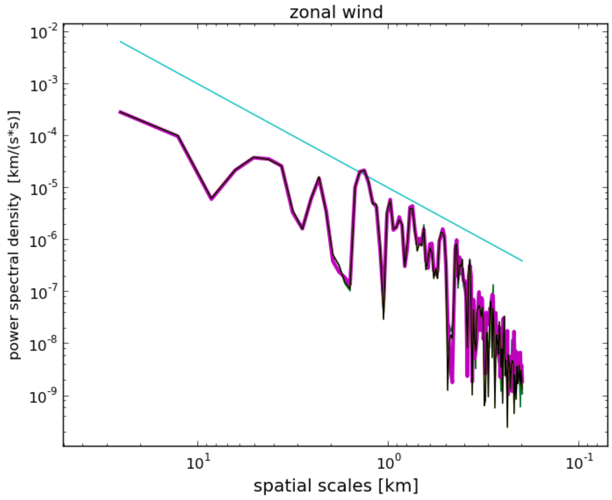

Figure 5.12: Vertical power spectral density distribution of the zonal wind profile between 30 km and 50 km for different temporal smoothing values of the positional data of launch 8 (0.06 s: blue, 1.06 s: thick violet, 4.06 s: black). The thick line indicates the chosen value in the further analysis. An arbitrary line with a slope of $k^{-\frac{5}{3}}$ has been added in cyan.

A contribution to the limited impact of the source data filtering lies in the vertical sampling of the profiles at a vertical resolution of 100 m. To illustrate the reasoning behind this value, figure 5.13 shows the numeric impact of the sampling interval on the spectral reproduction of the power spectral density distribution. It appears obvious that the lower values allow for better resolution of the high frequency dynamics. In fact, the entire analysis in this thesis has also been performed with a sampling value of 50 m. The evaluation of this data led to the conclusion that the spectral distributions between 30 km and 50 km are a special case, as the impact of the sampling at higher altitudes significantly increases the error spread. As a compromise between the wind reproduction at altitudes below and above 50 km, the value of 100 m has been chosen.

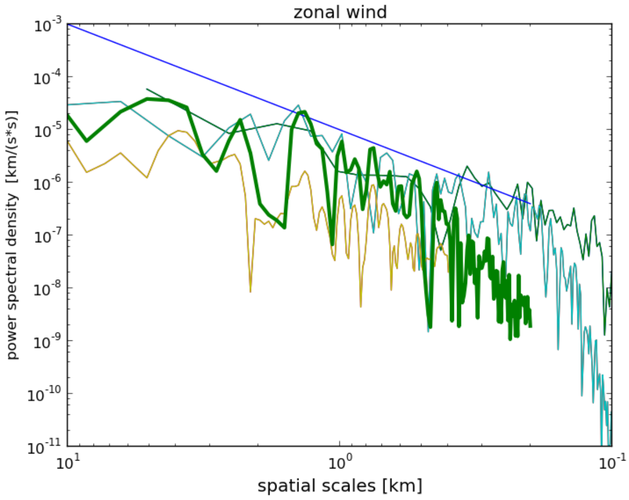

Figure 5.13: Vertical power spectral density distribution for different sampling values of the vertical zonal wind of launch 5 (20 m: green, 50 m: light blue, 100 m: thick green, 200 m: yellow). The thick line indicates the chosen value in the further analysis. An arbitrary line with a slope of $k^{-\frac{5}{3}}$ has been added in dark blue.

Taking the constraints of the analysis into account, the calculated power spectral density distribution of the datasonde soundings follow the expected inertial profile down to spatial scales of ≈ 0.3 km. The transition to noise appears to be on scales below 100 m for the altitude range of 30 km - 50 km. This indicates that the error estimate by the variance on 100 m scales is a valid approximation. Additional scale resolution is necessary to resolve the edges of the inertial subrange and calculate the inner and outer scale of the power spectrum. Instruments such as CONE and LITOS offer additional capabilities in this regard. (*Theuerkauf*, 2012; *Müllemann*, 2004).

6 Lidar measurements and method comparison

6.1 Wind profiles of the lidar measurements

Similar to section 5.2, the wind profiles of the lidar measurements made during the WADIS campaign on June 30th 2013 in a 2.5 h period are shown together in figure 6.1. They have been integrated over 30 min instead of the usual interval of 1 h in order to deliver independent data closely matched to the rocket launch timing (see table 6.1). After testing the NWT lidar azimuthal angle of 330° and the elevation angle of 30° during the first two launches, a closer match with the rocket trajectory was found in the azimuthal direction of 315°. The SET lidar was pointed during the entire campaign at an angle of 90° azimuth in the zonal direction and 20° elevation. The 150 m vertical resolution of the lidar wind data is affected by a 3 km running mean filter. Measurements were performed in daytime conditions representing significant processing challenges for the lidar data due to the use of an etalon as a wavelength filter in the DoRIS instrument during daytime (see also section 4.4.3) . The uncertainty of the background count rate during daytime is aa additional error source. The measurement uncertainty for a sounding volume at an altitude of 36 km with an integration time of 30 min is 6 m/s (*Hildebrand*, 2014). The error bars in the wind profiles are estimated using Poisson statistics and underestimate the real wind error range (see section 6.1.1). The data in the altitude range between 45 km and 55 km is assembled in a high sensitivity channel and allows therefore the highest possible accuracy in a comparison with the datasonde wind data. As can be seen in table 6.1, the wind error estimation of the NWT lidar measurements is below the benchmark of 6 m/s at the nearest point to the datasonde. Data below 45 km has been omitted due to the mentioned operational uncertainties. The lidar data was assembled by Gerd Baumgarten and Jens Hildebrand in support of this study. A summary of the lidar data in combination with the datasonde trajectories is shown in table 6.1.

launch number	date	start time [UTC]	near. altitude [km]	near. distance [km]	wind error [m/s]
5	30.06.13	22:41:28	53.9	0.5	3.8
6	30.06.13	23:26:13	49.6	3.9	3.9
7	30.06.13	23:57:41	53.2	1.4	3.8
8	01.07.13	00:36:45	53.1	0.7	3.9
9	01.07.13	01:09:28	54.5	1.9	4.4

Table 6.1: Table of 30 min NWT and SET lidar integration start times and corresponding rocket launches. Nearest distance between datasonde and NWT lidar beam and 30 min NWT wind error at nearest altitude is also given.

The mean profile shown in figure 6.1 is calculated twice, once including the wind data from launch 5, and once without. The NWT lidar shows a highly irregular wind spike at 47 km. In order to minimize the influence of unphysical outliers, a seperate evaluation has been performed.

The zonal wind features several westward wind spikes at 64 km, 58 km and 52 km respectively. The ECMWF data shows none of these features and does not appear to be underresolved, leading to the assumption of several independent local wind layers. The line-of-sight wind profile follows the ECMWF more closely, with the exception of a spike at 65 km altitude. The addition of the data from launch 5 seems to smooth the layering, which leads to the conclusion that these results are inconsistent with the other measurements in a close time period.

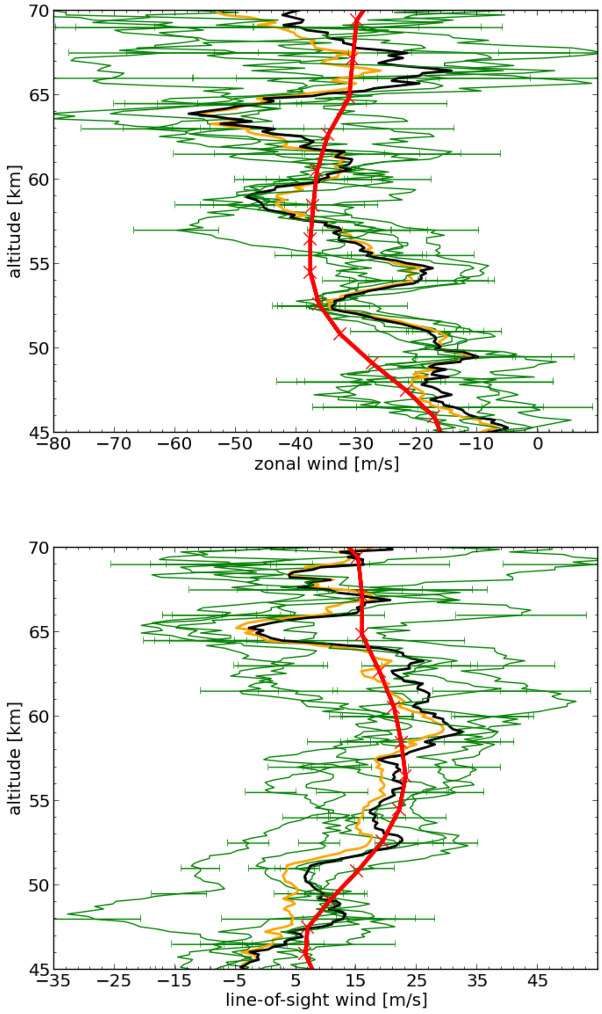

Figure 6.1: Common plot of lidar measurements during launches 5, 6, 7, 8 and 9, which occurred in a 2.5 h window. The mean profile including the outlier launch 5 is shown in orange, while the mean profile without launch 5 is shown in black. For comparison, the ECMWF data of the 01.07.2013 at 12 am has been added in red, with crosses at the modeled data points. All lidar profiles compared to the datasonde measurements are found in the appendix 8.1.

Separating the lidar wind profiles according to the rocket launch times shows a greater variability of the wind data compared to the datasonde soundings (see figure 6.2). Launches 6,7 and 8,9 were performed in a 30 min interval (see table 5.1) leading to a crossing of the zonal wind profiles above 62 km altitude. Assuming static wind, a parallel evolution of the profile is expected, making the wind reversals at 47 km, 60 km and 66 km implausible. The wind profiles of the NWT lidar appear more consistent, but still showing wind reversals at 47 km, 51 km, 55 km, 60 km and 66 km. None of these qualitative features are born out in the datasonde data, leading to questions about the systematic sources of error in the lidar data.

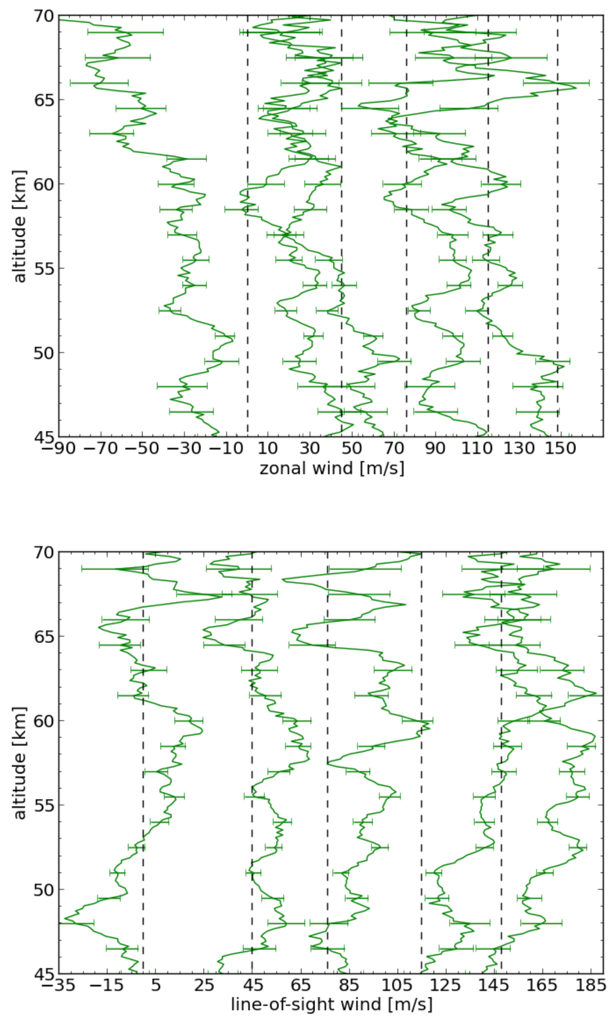

Figure 6.2: Common plot of lidar measurements during launches 5, 6, 7, 8 and 9, which occurred in a 2.5 h window. The wind axis is correct for the first profile from the left, while each successive profile is shifted by +1 along the x-axis per minute time difference. The dashed line represents the origin relative to the profile.

6.1.1 Error discussion

The systematic sources of error in the lidar wind measurements are difficult to quantify if a bias in the photon count statistics exists. The unusually short integration time leads to low backscatter and in consequence low photon count rates. The wind derivation also depends on the temperature profile calculated from hydrostatic integration of a given start temperature (*Baumgarten*, 2010). While the associated error decreases with altitude, in the considered range of 45 km - 70 km it might lead to a systematic bias.

Other sources of bias are the instrumental calibrations: Some parameters are variable and constantly monitored during measurement, such as the frequency of the emitted light, which has a variability of 50 MHz leading to a possible maximum error of 12 m/s, while other parameters are assumed constant and set at irregular intervals, such as the mechanical adjustment of the optical bank, in which a 2% misalignment leads to a 10 m/s error, or the tuning of the spectral filter for daytime measurements.

The vertical wind w_z has been presumed to be negligible for both the datasonde and lidar data (see section 4.3.2). As the line-of-sight directions of the NWT and SET lidar are both at an off-zenith angle, the contribution of the vertical wind leads to an erroneous horizontal wind projection. Based on prior studies, a vertical wind speed $w_z < 2$ m/s with a similar spatial and temporal variability is assumed (*Hildebrand*, 2014). An error range of 3.5 m/s (see table 6.1) and an off-zenith angle θ of 20° is assumed in the following calculations. Projecting this error range on the horizontal plane for $w_z = 0$ leads to a horizontal measurement uncertainty of $\Delta w_{xy} \approx 10$ m/s. Assuming a vertical wind $w_z < 2$ m/s, this error range increases to $w_{xy} \approx 15$ m/s. Absent any vertical wind data, it is impossible to accurately project the off-zenith wind components on the horizontal plane, therefore an approach developed by *Liu et al.* (2002), which uses the projection of the first approach in conjuntion with the wind variability of the second, estimates the wind uncertainty at $w_z \approx 12$ m/s.

6.2 Result comparison

6.2.1 Comparison of RMR-Lidar and datasonde wind measurements

An exemplary comparison of the lidar and datasonde wind measurements during rocket launch 8 together with ECMWF model- and Saura MF radar data can be seen in figure 6.3. Launch 8 has been chosen due to the close proximity of the datasonde to the NWT lidar beam (see figure 5.4) and the availability of Saura MF radar wind data (see section 4.5). The full figures are found in 8.1. The altitude range of 45 - 70 km has been chosen as the lidar wind has its highest sensitivity in the applicable detection channels (see section 6.1). The comparison of the line-of-sight wind of the NWT lidar has been made with a projection of the datasonde horizontal wind components towards the NWT azimuthal angle along the earth's surface. The influence of vertical wind on the difference in wind sounding direction is discussed in section 6.1.1.

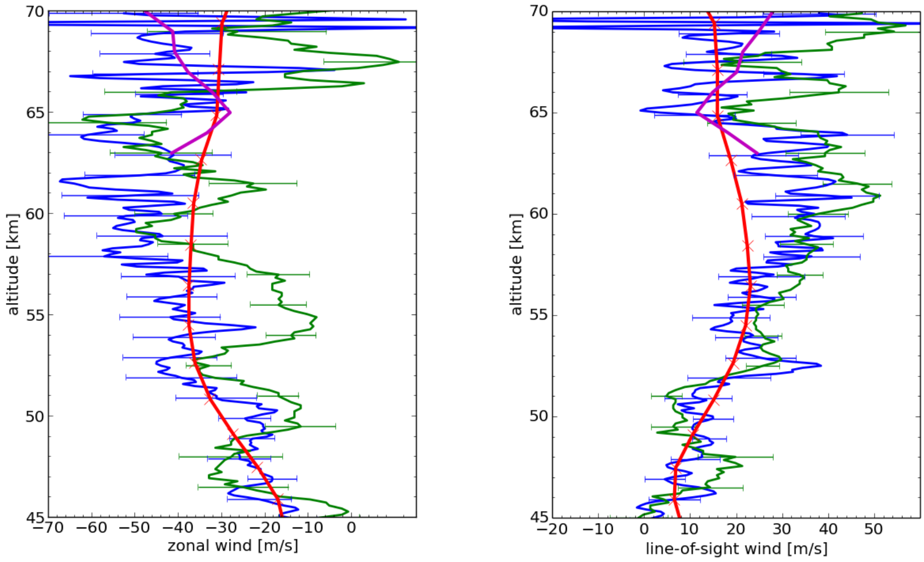

Figure 6.3: Comparison of datasonde (blue) and lidar (green) wind measurements after rocket launch 8. For comparison, the ECMWF data of the 01.07.2013 at 0 UT has been added in red. Additionally, the wind data from the Saura MF radar at 0.15 UT is shown in violet.

To account for the wind variability, the mean of the 5 launches in 2.5 h during the 30.06./01.07.2013 is shown in figure 6.4. The mean of the Saura MF-Radar wind measurements during launches 8 and 9 in conjunction with the ECMWF model data has been added to the figures. The datasonde wind mean has been post-processed with a 3 km running mean similar to the lidar data and the lidar mean excludes launch 5 (see section 6.1). The error bars are calculated using Gauss error propagation of the source data sets (*Grabe*, 2010). They do not appear centered on the mean as a result of the additional smoothing performed. The datasonde mean is only available below 65 km due to the lower starting altitude of the launch 6 sounding (see section 8.3). Both the zonal and the line-of-sight wind means show qualitative agreement inside the respective error ranges.

In the zonal case, lower westward wind speeds at 61 km and 55 km point to the spatial variability of the SET lidar and datasonde soundings in the eastward and westward direction (see section 5.1.2). The ECMWF model wind data does not show any wind variability in the altitude range, which appears unusual for the middle atmosphere. Low model resolution does not appear to be the reason, as the ECMWF data is sampled evenly every 1 km in the vertical direction, pointing a possible flaw in the spectral representation of the underlying dynamics. Smoothing the zonal wind profiles further should yield a qualitatively similar curvature. The zonal Saura MF data follows a similar profile to the SET lidar in its altitude range, with a wind minimum at 65 km instead of 67 km. The mean datasonde wind is available for comparison below 65 km and shows a similar vertical gradient inside its error range.

In the case of NWT line-of-sight winds, the agreement between lidar and datasonde wind soundings appears to be substantial, showing similar wind profile features at 63 km, 59 km, 53 km and 51 km inside ranges of ± 2 m/s, below the respective error ranges. As in the zonal case, the ECMWF curvature matches both wind profiles and the Saura MF radar wind data matches the lidar wind with a wind maximum at 65 km.

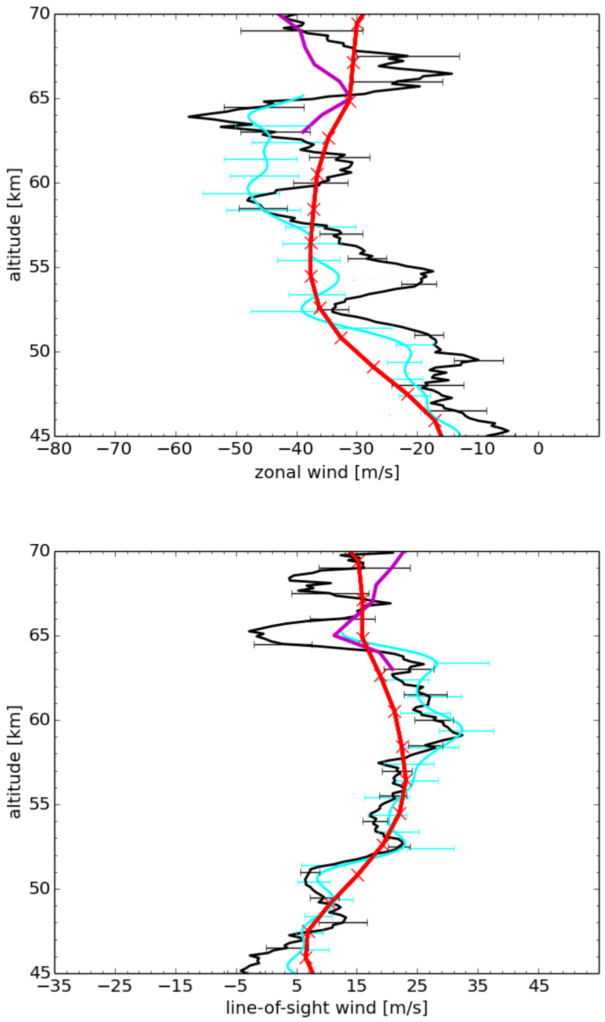

Figure 6.4: Comparison of the mean datasonde (cyan) and lidar (black) wind measurements on the 30.06./01.07.2013. For comparison, the ECMWF data of the 01.07.2013 at 0 UT has been added in red.

In order to analyze the agreement quantitatively, the correlation of the measurements of both methods serve as a useful tool in the analysis. The results of the wind speed measurements through datasonde and lidar soundings are shown together for altitudes between 50 km and 60 km in figure 6.5. The full figures for other altitude ranges can be found in section 8.2. A maximum altitude of 60 km has been chosen to minimize datasonde wind noise below 60 km. Ideally, a relationship of 1:1 points to a complete agreement of the wind sounding methods, meaning two independent methods confirm the physical condition inside comparable error ranges and allow a choice according to the requirements of the researcher. To judge the wind measurement accuracy of either method, the linear regression through the data points at different altitude ranges is shown in table 6.2 in addition to the mean wind error of the included data points. While the lidar data has not been used in the wind profiles below 45 km altitude, it has been included in these statistics in order to make a qualitative judgment as to the relation between altitude and data quality. Only data points at a common altitude of lidar (150 m, see 6.1) and datasonde spline sampling (100 m, see 5.1.3) have been used. The regression is not weighted according to the error bars, instead the mean error inside the height interval is given. The datasonde wind data has been projected in the line-of-sight direction of the NWT lidar from the zonal and meridional components. The data can be compared because the datasonde is closest to the beam, and the NWT lidar has the highest accuracy, in the same altitude range: 45 km - 55 km (see table 6.1). The zonal data does not share a common sounding volume, yet the comparison is still useful: While the agreement of the line-of-sight data seems to deteriorate with altitude, the agreement of the zonal data improves. In both cases the error range of the datasonde decreases with altitude as a result of the reduced variability in the position data, while the accuracy of the lidar data increases with altitude due to the higher sensitivity in the detection channel. The accuracy of both methods is improved in the case of line of sight measurements. The common sounding volume can't be responsible, as the error calculations are separate. The agreement of the correlation, on the other hand, is highest in the region of closest proximity. The significance of the agreement improves with more datapoints in the 40 km - 60 km range, pointing to a stable result across a distance between lidar beam and datasonde of the order of 10 km. A correlation between lidar and datasonde wind soundings of ≈1 at different altitudes for zonal and line-of-sight data is a promising first result.

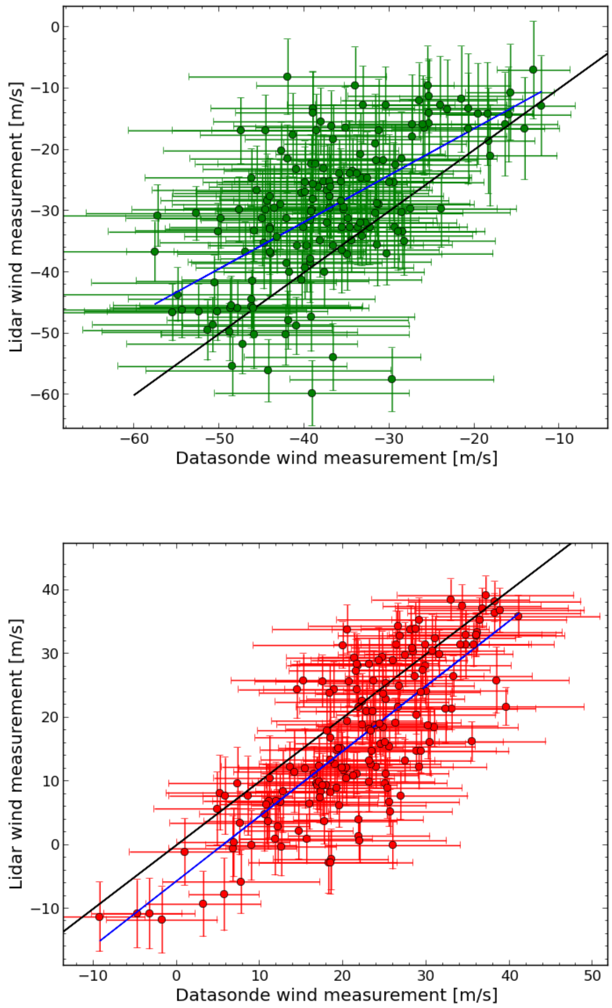

Figure 6.5: Correlation plot in the altitude range between 50 and 60 km of launches 5, 6, 7, 8 and 9. The result of the lidar wind measurement at a given altitude is shown against the result of the datasonde wind measurement. On top are the results of the zonal measurements by the SET telescope, while the results of the NWT telescope in the rocket launch direction are at the bottom. A blue line shows the linear regression through the data points, while a black line shows the ideal 1:1 relationship. The results of the regression are found in table 6.2. The error bars are taken from the respective data analysis.

altitude range [km]:	50-60	40-60	30-50
zonal correlation	0.76	0.73	1.06
correl. std. dev.	0.08	0.05	0.2
mean datasonde wind error [m/s]	11.58	8.69	4.33
mean SET lidar error [m/s]	6.41	8.59	9.90
line-of-sight correlation	1.02	0.94	0.54
correl. std. dev.	0.07	0.05	0.1
mean datasonde wind error [m/s]	8.24	6.35	3.35
mean NWT lidar error [m/s]	4.61	5.90	6.69

Table 6.2: Fit values of a linear regression performed on the corresponding wind speed values of lidar and datasonde measurements in several common altitude ranges. Error bars are not weighted, therefore the mean of the error is given. Ideal correlation is 1.

6.2.2 Comparison to literature data

In order to compare the resulting wind profiles with prior studies and theoretical models, any wind data is required to originate from a similar latitude (69° N) and a similar timeframe (summer) to the WADIS campaign, as the annual variability of the atmospheric wind structure (see section 2.3) has a severe impact on the experimental outcome. In a study by *Müllemann* (2004), the results of the falling sphere wind measurements conducted in 1987 and 2001 during the MAC/SINE and MIDAS/SOLSTICE campaigns have been averaged and compared to the theoretical ECMWF-, COMMA/IAP- and HWM-93-models (*Lübken et al.*, 1990; *Müllemann et al.*, 2003; *Molteni et al.*, 1996; *Berger*, 2002; *Drob et al.*, 2008). As part of the campaigns, 22 rockets were launched at the Andøya Rocket Range inside a timeframe of ±2 weeks of the summer solstice. The summer solstice occured in 2013 on the 21.06., i.e. inside the timeframe of the prior study, therefore these results have been used as a reference for the WADIS lidar and rocket soundings.

Figure 6.6 shows the comparison for the zonal and meridional winds. The lidar wind data between 45 km and 70 km is only shown for the zonal wind, as a lack of source data hinders a reprojection of the wind components in the NWT lidar direction, as has been performed in section 6.2.1.

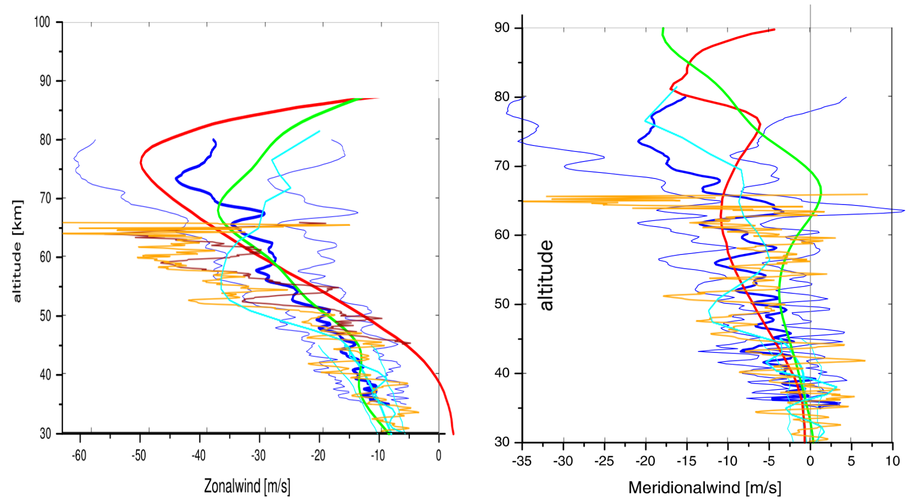

Figure 6.6: Zonal and meridional wind data of the MAC/SINE (1987), MIDAS/SOLSTICE (2001) and WADIS (2013) falling sphere and datasonde measurements. Mean winds for the time period of ± 2 weeks around the summer solstice of 1987 and 2001 are shown in dark blue, with the variability ranges indicated by a thin blue line. The datasonde mean of the WADIS campaign is shown in orange and the mean of the zonal lidar winds in brown. ECMWF (cyan), COMMA/IAP (red) and HWM93 (light green) model data is shown. Figures adapted from *Müllemann* (2004).

The mean of the zonal datasonde wind data follows the historical mean profile inside its range of variability up to an altitude of ≈ 50 km, above which significantly higher westward wind speeds of 40 m/s - 50 m/s are observed. A similar anomaly is observed for the lidar measurement at ≈ 60 km. As the ECMWF model data generated for WADIS conditions at 69°N also reaches a wind speed of 40 m/s at 55 km altitude, this points to an influence of the local wind condition in conflict with the historical measurements. At the same time, the mean profiles for both the lidar and datasonde data have been restritcted to a range below 66 km representing an error range of 20 m/s, compared to a spread < 20 m/s of the *Müllemann* (2004) wind data at this altitude, showing the significant variability of the WADIS soundings at high altitudes.

For the meridional wind, mean measurements outside the variability range of the *Müllemann* (2004) measurements are observed for the entire altitude range. The data has also been restricted to a range below 66 km, representing an error range of 15 m/s. At 64 km, the variability of the comparison data set ranges up to 25 m/s, therefore its data is considered only below that altitude.

In the WADIS data set, northward wind flows of a strength ≈ 5 m/s at 42 km and 44 km are followed by a strong southward flowing wind layer at ≈ 50 km with ≈ -20 m/s and a still layer with ≈ 0 m/s at 60 km. A qualitative comparison with the meridional ECMWF data shows similar features at 38 km, 49 km and 55 km. The study of previous data appears to show a different segmentation of horizontal wind layers with southward flows from -10 m/s to -15 m/s at 43 km, 56 km and 62 km altitude and layers of low wind speed between -5 m/s and 0 m/s at 50 km, 54 km and 57 km altitude.

Apart from a confirmation of the general summer polar wind profile (see section 2.3), no further conclusions about the validity of the WADIS data set can be made from its comparison to the falling sphere measurements of the MAC/SINE and MIDAS/SOLSTICE campaigns.

7 Summary and Conclusion

Before this study, lidar and datasonde wind measurements have never been conducted simultaneously and in a quasi common volume. The opportunity to compare both methods for the first time during the summer WADIS campaign in Andøya, Norway has been the origin of this study.

As part of this study, a new datasonde analysis software designed to handle a higher radar tracking resolution of 50 Hz has been developed and compared to previous computational methods. The high resolution of the source data allowed an improved estimation of the datasonde wind errors. Despite the higher resolution of the new software, the analysis is consistent with previous analysis methods with a difference of less than 0.6 m/s under certain conditions (see section 5.3.2).

Taking only the most reliable lidar data on the night of the 30.06. / 01.07.2013 into account, a close agreement between the lidar and datasonde wind measurements has been shown in the altitude range between 45 km and 65 km. In the specific case of the rocket launch on the 01.07.2013 at 0:30 UT, the comparison of lidar, datasonde and MF radar wind measurements show excellent agreement in the altitude range of 45 km - 70 km. We find a better agreement in the line-of-sight wind measurements of the NWT lidar telescope, as its direction points close to the datasonde trajectory, than in the zonal wind measurements of the SET lidar telescope, whose sounding volumes are separated by more than 20 km along the circle of latitude.

The new analysis software is available for use during the upcoming WADIS-II campaign planned for the winter months of 2014. Night-time conditions will allow to focus on comparisons between the lidar and datasonde uncertainties below 45 km. The high cadence of rocket launches should be kept, as they allow to identify persistent and likely larger scale features in the wind profile.

8 Appendix

8.1 Comparison of lidar and datasonde wind measurements

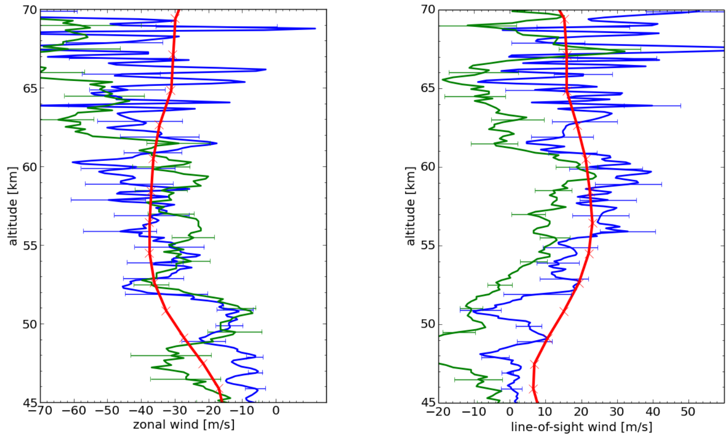

Figure 8.1: Comparison of datasonde (blue) and lidar (green) wind measurements after rocket launch 5. For comparison, the ECMWF data of the 01.07.2013 at 0 UT has been added in red.

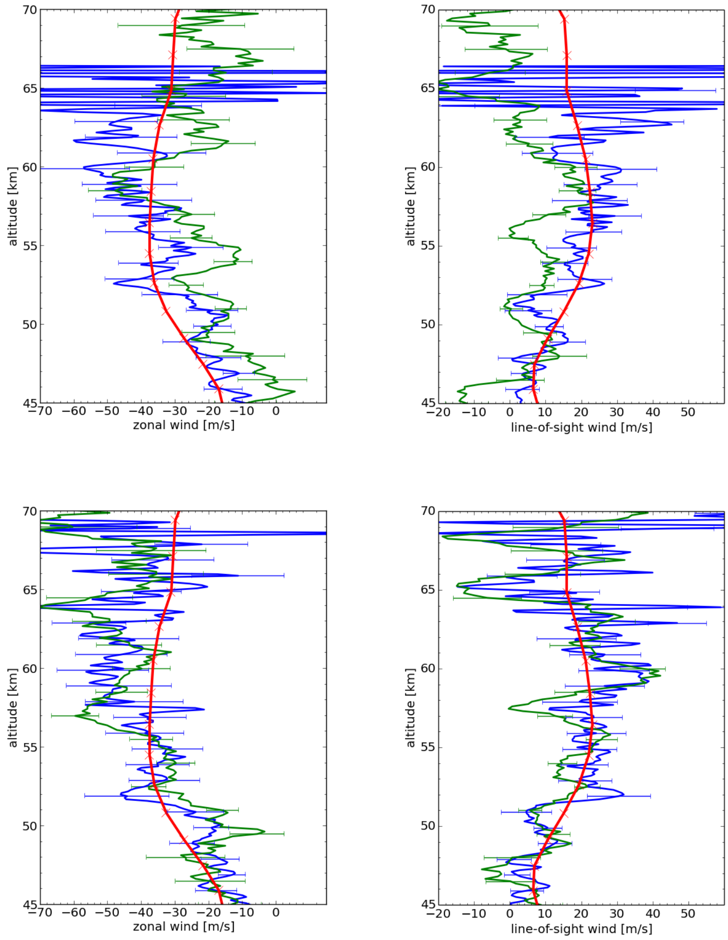

Figure 8.2: Comparison of datasonde (blue) and lidar (green) wind measurements after rocket launches 6 (top) and 7 (bottom). For comparison, the ECMWF data of the 01.07.2013 at 0 UT (both profiles) has been added in red.

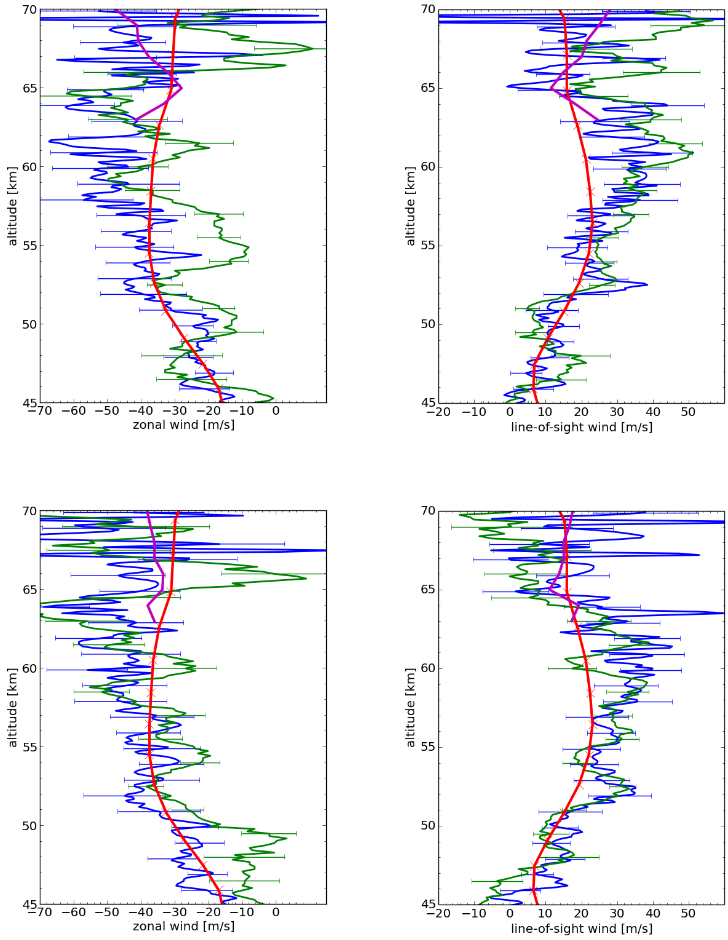

Figure 8.3: Comparison of datasonde (blue) and lidar (green) wind measurements after rocket launches 8 (top) and 9 (bottom). For comparison, the ECMWF data of the 01.07.2013 at 0 UT (both profiles) has been added in red. Additionally, the wind data from the Saura MF radar at 0.15 UT (top) and 0.45 UT (bottom) is shown in violet.

8.2 Correlation of lidar and datasonde wind measurements

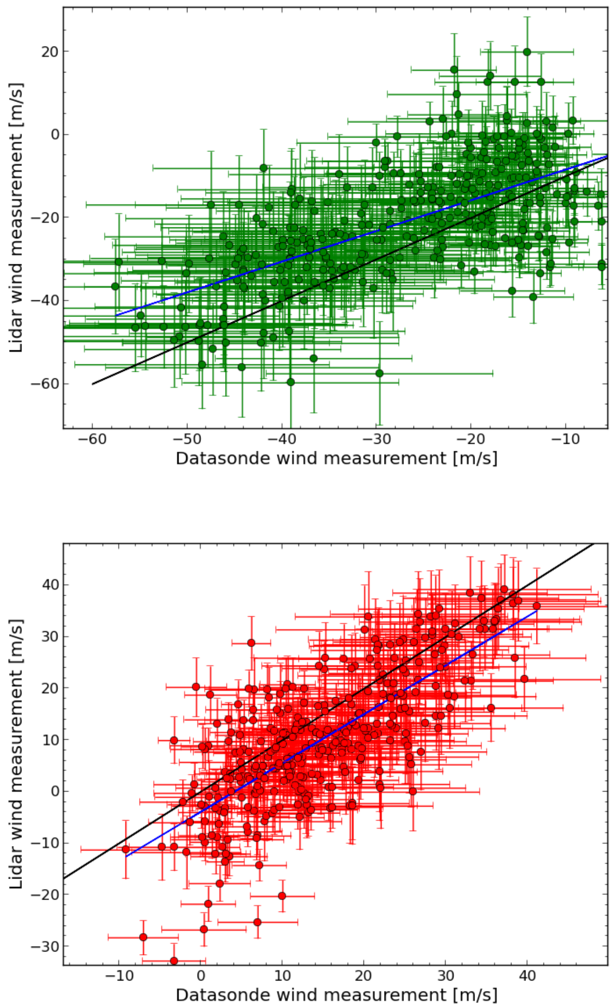

Figure 8.4: Correlation plot in the altitude range between 40 and 60 km of launches 5, 6, 7, 8 and 9. The result of the lidar wind measurement at a given altitude is shown against the result of the datasonde wind measurement. On top are the results of the zonal measurements by the SET telescope, while the results of the NWT telescope in the rocket launch direction are at the bottom. A blue line shows the linear regression through the data points, while a black line shows the ideal 1:1 relationship. The results of the regression are found in table 6.2. The error bars are taken from the respective data analysis.

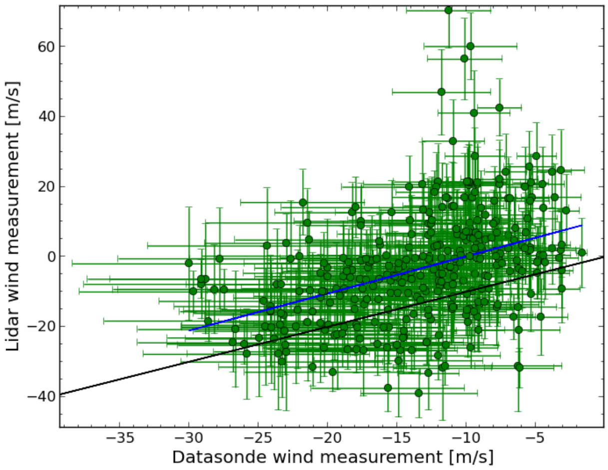

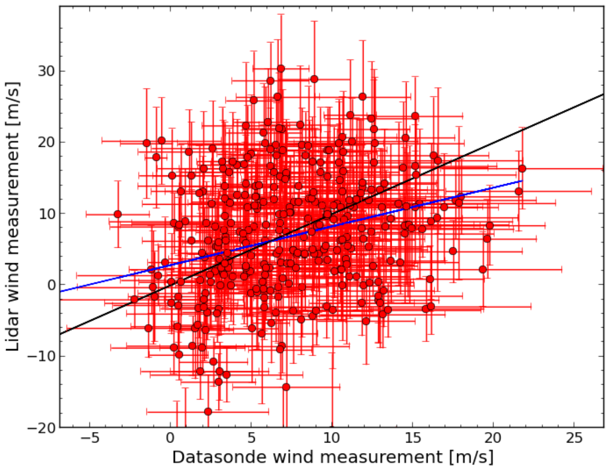

Figure 8.5: Correlation plot in the altitude range between 30 and 50 km of launches 5, 6, 7, 8 and 9. The result of the lidar wind measurement at a given altitude is shown against the result of the datasonde wind measurement. On top are the results of the zonal measurements by the SET telescope, while the results of the NWT telescope in the rocket launch direction are at the bottom. A blue line shows the linear regression through the data points, while a black line shows the ideal 1:1 relationship. The results of the regression are found in table 6.2. The error bars are taken from the respective data analysis.

8.3 Datasonde wind measurements

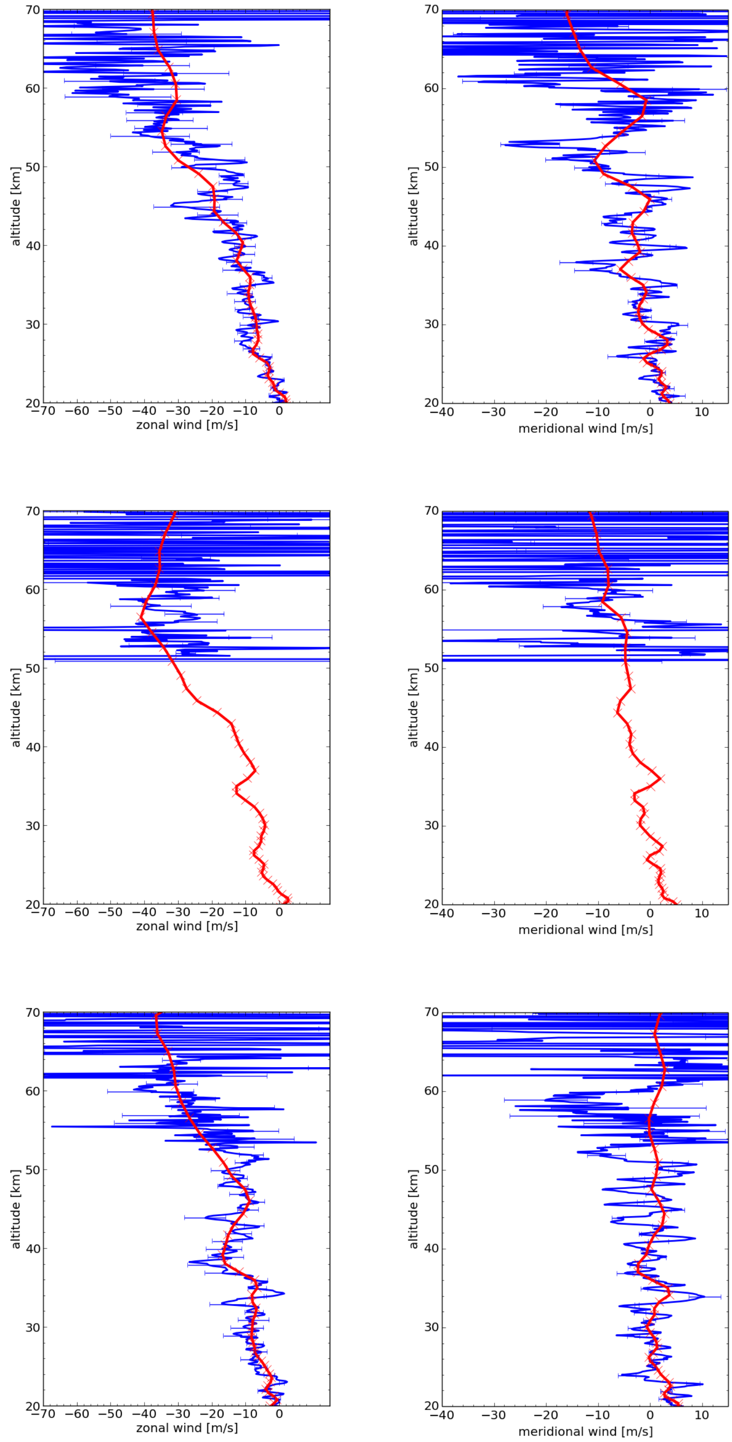

Figure 8.6: Wind profiles of meteorological rocket launch 1 (top), launch 2 (middle) and launch 3 (bottom) in blue For comparison, the ECMWF data of the 27.06.2013 at 0 UT (top), the 28.06.2013 at 0 UT (middle) and 29.06.2013 at 18 UT (bottom) has been added in red.

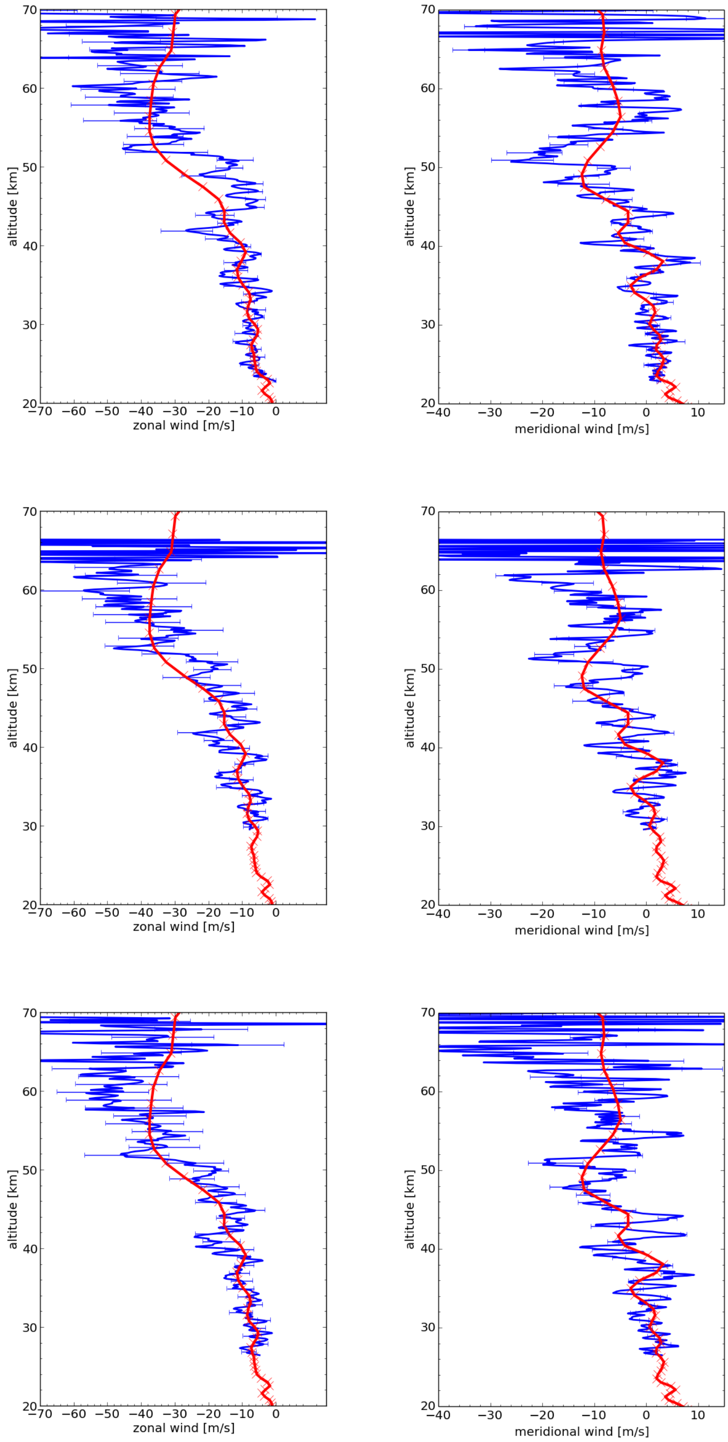

Figure 8.7: Wind profiles of meteorological rocket launch 5 (top), launch 6 (middle) and launch 7 (bottom) in blue. For comparison, the ECMWF data of the 01.07.2013 at 0 UT (all profiles) has been added in red.

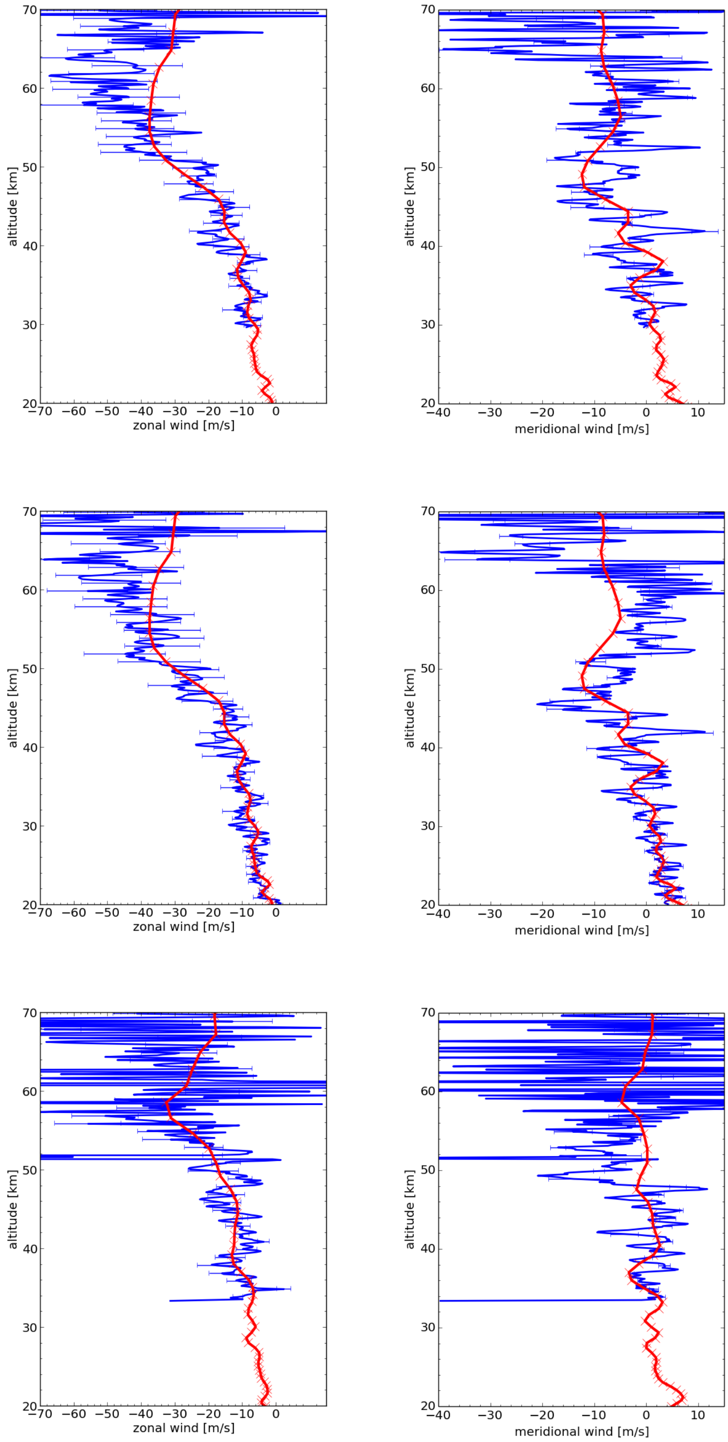

Figure 8.8: Wind profiles of meteorological rocket launch 8 (top), launch 9 (middle) and launch 11 (bottom) in blue. For comparison, the ECMWF data of the 01.07.2013 at 0 UT (top and middle) and 18 UT (bottom) has been added in red.

Bibliography

Altenbuchner, L., J. Ettl, M. Hörschgen, and W. Jung, MORABA–Overview on DLR's Mobile Rocket Base and Projects, in *SpaceOps 2012 Conference Proceedings*, 2012.

Ambaum, M. H. P., *Thermal Physics of the Atmosphere*, John Wiley & Sons, 2010.

Baumgarten, G., Doppler Rayleigh/Mie/Raman lidar for wind and temperature measurements in the middle atmosphere up to 80 km, *Atmospheric Measurement Techniques*, *3*(6), 1509–1518, 2010.

Baumgarten, G., private communication, 2014.

Becker, R., Temperatur- und Windmessungen mit Fallenden Kugeln während der Kampagne ECHO-94/ Rolf Becker, 1995.

Bendat, J. S., and A. G. Piersol, *Random Data*, Analysis and Measurement Procedures, John Wiley & Sons, 2011.

Berger, U., Icy particles in the summer mesopause region: Three-dimensional modeling of their environment and two-dimensional modeling of their transport, *Journal of Geophysical Research*, *107*(A11), 1366, 2002.

Brekke, A., *Physics of the Upper Polar Atmosphere*, Springer, 2012.

Carter, R. T., P. S. Jandir, and M. E. Kress, Estimating the drag coefficients of meteorites for all Mach number regimes, in *th Lunar and Planetary Science Conference*, 2009.

Chapman, S., and R. S. Lindzen, *Atmospheric Tides*, Thermal and Gravitational, Springer, 1970.

Drob, D. P., J. T. Emmert, G. Crowley, J. M. Picone, G. G. Shepherd, W. Skinner, P. Hays, R. J. Niciejewski, M. Larsen, C. Y. She, J. W. Meriwether, G. Hernandez, M. J. Jarvis, D. P. Sipler, C. A. Tepley, M. S. O'Brien, J. R. Bowman, Q. Wu, Y. Murayama, S. Kawamura, I. M. Reid, and R. A. Vincent, An empirical model of the Earth's horizontal wind fields: HWM07, *Journal of Geophysical Research*, *113*(A12), A12,304, 2008.

Durbin, P. A., and B. A. P. Reif, *Statistical Theory and Modeling for Turbulent Flows*, John Wiley & Sons, 2011.

Eddy, A., F. M. Haase, and D. R. Haragan, Determination of winds from meteorological rocketsondes, 1965.

Engler, N. A., Development of Methods to Determine Winds, Density, Pressure, and Temperature from the Robin Falling Balloon, 1965.

Finlayson-Pitts, B. J., and J. James N Pitts, *Chemistry of the Upper and Lower Atmosphere*, Theory, Experiments, and Applications, Academic Press, 1999.

Fritts, D. C., Gravity wave dynamics and effects in the middle atmosphere, *Reviews of Geophysics*, *41* (1), 1003, 2003.

Grabe, M., *Generalized Gaussian Error Calculus*, Springer, 2010.

Grzegorzewski, J., Auswirkung der Teleskop-Überlappfunktion auf die Datenqualität eines Rayleigh/Mie/Raman-Lidar Instruments, 2013.

Harris, F. J., On the use of windows for harmonic analysis with the discrete Fourier transform, *Proceedings of the IEEE*, *66* (1), 51–83, 1978.

Heisenberg, W., Zur statistischen Theorie der Turbulenz, *Zeitschrift für Physik*, *124* (7-12), 628–657, 1948.

Hildebrand, J., Wind and Temperature Measurements by Doppler Lidar in the Arctic Middle Atmosphere, 2014.

Hildebrand, J., G. Baumgarten, J. Fiedler, U. P. Hoppe, B. Kaifler, F.-J. Lübken, and B. P. Williams, Combined wind measurements by two different lidar instruments in the Arctic middle atmosphere, *Atmospheric Measurement Techniques*, *5* (10), 2433–2445, 2012.

Hocking, W. K., Strengths and limitations of MST radar measurements of middle-atmosphere winds, *Annales Geophysicae*, 1997.

Kalteis, X. M., Dlr's new tracking radar, *Proceedings of the 11th ESA Symposium on European Rocket and Balloon Programmes and Related Research, Montreux, Switzerland,p. 293–295*, 1993.

Kasting, J. F., Earth's early atmosphere, *Science*, 1993.

Kent, G. S., and R. Wright, A review of laser radar measurements of atmospheric properties, *Journal of Atmospheric and Terrestrial Physics*, 1970.

Kolmogoroff, A., *The local structure of turbulence incompressible viscous fluid for very large Reynolds number*, Turbulence, 1941.

Larsen, M. F., A. Z. Liu, R. L. Bishop, and J. H. Hecht, *TOMEX: A comparison of lidar and sounding rocket chemical tracer wind measurements*, Geophysical research letters, 2003.

Leviton, R., and J. B. Wright, Accuracy of density from the Robin falling sphere, 1961.

Liu, A. Z., W. K. Hocking, S. J. Franke, and T. Thayaparan, Comparison of Na lidar and meteor radar wind measurements at Starfire Optical Range, NM, USA, *Journal of Atmospheric and Solar-Terrestrial Physics*, *64* (1), 31–40, 2002.

Lübken, F.-J., Experimental results on the role of turbulence for the heat budget of the upper atmosphere, 1993.

Lübken, F.-J., U. von Zahn, A. Manson, and C. Meek, Mean state densities, temperatures and winds during the MAC/SINE and MAC/EPSILON campaigns, *Journal of Atmospheric and Terrestrial Physics*, *52*(10-11), 955–970, 1990.

Lübken, F.-J., W. Hillert, G. Lehmacher, and U. von Zahn, Intercomparison of density and temperature profiles obtained by lidar, ionization gauges, falling spheres, datasondes and radiosondes during the DYANA campaign, *Journal of Atmospheric and Terrestrial Physics*, *56*(13-14), 1969–1984, 1994.

MM2sp, (own work) [public domain], via wikimedia commons: http://upload.wikimedia.org/wikipedia/commons/4/44/rocketrangesummer.jpg, 2014.

Molteni, F., R. Buizza, T. N. Palmer, and T. Petroliagis, The ECMWF Ensemble Prediction System: Methodology and validation, *Quarterly Journal of the Royal Meteorological Society*, *122*(529), 73–119, 1996.

Müllemann, A., Temperaturen, Winde und Turbulenz in der polaren Sommermesosphäre, 2004.

Müllemann, A., M. Rapp, and F.-J. Lübken, Morphology of turbulence in the polar summer mesopause region during the MIDAS/SOLSTICE campaign 2001, *Advances in Space Research*, *31*(9), 2069–2074, 2003.

Murayama, Y., K. Igarashi, and I. Nishimuta, Wind observations in the MLT region over Southern Japan, by using foil chaff technique, Yamagawa MF radar and the NW radar, *Advances in Space Research*, 1999.

Philbrick, C. R., A. C. Faire, and D. H. Fryklund, Measurements of Atmospheric Density at Kwajalein Atoll, 18 May 1977, 1978.

Philbrick, C. R., F. J. Schmidlin, and K. U. Grossmann, Density and temperature structure over northern Europe, *Journal of Atmospheric and Terrestrial Physics*, 1985.

Picone, J. M., A. E. Hedin, D. P. Drob, and A. C. Aikin, NRLMSISE-00 empirical model of the atmosphere: Statistical comparisons and scientific issues, *Journal of Geophysical Research: Atmospheres (1984–2012)*, *107*(A12), SIA 15–1–SIA 15–16, 2002.

Salby, M. L., *Fundamentals of Atmospheric Physics*, Academic Press, 1996.

Schmidlin, F. J., Rocket techniques used to measure the neutral atmosphere, *In International Council of Scientific Unions Handbook for MAP, Vol. 19 28 p (SEE N86-26725 17-46)*, *19*, 1986.

Schmidlin, F. J., H. S. Lee, and W. Michel, The inflatable sphere: A technique for the accurate measurement of middle atmosphere temperatures, *Journal of Geophysical Research*, 1991.

Schöch, A., Thermal Structure and Gravity Waves in the Arctic Middle Atmosphere Above ALOMAR (69.3°N, 16.0°E), 2007.

Shah, A., *Development of a Falling Sphere Instrument for High-resolution Neutral Wind Measurements in the Mesosphere and Lower Thermosphere*, ProQuest, 2009.

Singer, W., R. Latteck, and D. A. Holdsworth, A new narrow beam MF radar at 3 MHz for studies of the high-latitude middle atmosphere: System description and first results, in *Proceedings of the Tenth International Workshop on Technical and Scientific Aspects of MST Radar MST*, 2003.

Space Data Corporation, Meteorological Sounding Rocket Systems, 1998.

Suits, B. H., Super loki starute, http://www.phy.mtu.edu/rocket/starute.html, 2014.

Tatarskii, V. I., The effects of the turbulent atmosphere on wave propagation, *Israel Program for Scientific Translations*, 1971.

Theuerkauf, A., Stratospheric Turbulence Observations with the New Balloon-borne Instrument LITOS, 2012.

Visconti, G., *Fundamentals of Physics and Chemistry of the Atmosphere*, Springer, 2001.

Wong, S., Temperatur- und windmessungen in der polaren mesospäre während der tramp/temperature-kampagne, 1998.

Zimmerman, S. P., and E. A. Murphy, Stratospheric and Mesospheric Turbulence, in *Dynamical and Chemical Coupling Between the Neutral and Ionized Atmosphere*, pp. 35–47, Springer Netherlands, Dordrecht, 1977.

9 Acknowledgements

I would like to thank:

- My parents, for the support they gave me during my studies.
- Gerd Baumgarten, without whose patient help I would never have been able to finish this thesis.
- Jens Hildebrand, for his practical advice and data analysis.
- Prof. Lübken, for offering me the project and a place at the IAP.
- And everyone else who contributed to this work.